

BRNO UNIVERSITY OF TECHNOLOGY

Faculty of Mechanical Engineering

MASTER'S THESIS

Brno, 2018

Bc. Jakub Drahotský



BRNO UNIVERSITY OF TECHNOLOGY

VYSOKÉ UČENÍ TECHNICKÉ V BRNĚ

FACULTY OF MECHANICAL ENGINEERING

FAKULTA STROJNÍHO INŽENÝRSTVÍ

INSTITUTE OF PHYSICAL ENGINEERING

ÚSTAV FYZIKÁLNÍHO INŽENÝRSTVÍ

**TEMPERATURE PROFILES AND TEMPERATURE
FLUCTUATIONS IN TURBULENT RAYLEIGH-BÉNARD
CONVECTION**

TEPLOTNÍ PROFILY A FLUKTUACE TEPLoty V TURBULENTNÍ RAYLEIGHOVĚ-BÉNARDOVĚ KONVEKCI

MASTER'S THESIS

DIPLOMOVÁ PRÁCE

AUTHOR

AUTOR PRÁCE

Bc. Jakub Drahotský

SUPERVISOR

VEDOUCÍ PRÁCE

Ing. Pavel Urban, Ph.D.

BRNO 2018



This diploma thesis was elaborated at the
Institute of Scientific Instruments of the AS CR, v. v. i.

Master's Thesis Assignment

Institut: Institute of Physical Engineering
Student: **Bc. Jakub Drahotský**
Degree program: Applied Sciences in Engineering
Branch: Physical Engineering and Nanotechnology
Supervisor: **Ing. Pavel Urban, Ph.D.**
Academic year: 2017/18

As provided for by the Act No. 111/98 Coll. on higher education institutions and the BUT Study and Examination Regulations, the director of the Institute hereby assigns the following topic of Master's Thesis:

Temperature profiles and temperature fluctuations in turbulent Rayleigh-Bénard convection

Brief description:

Modelling of large-scale thermally-generated turbulent flows (such as in Earth's atmosphere, oceans, or Sun) is approached in laboratory experiments on the basis of a simplified model system called the Rayleigh-Bénard convection (RBC). The RBC occurs in a fluid layer confined between two horizontal perfectly conducting plates heated from below and cooled from above due to the buoyancy in the gravitational field. The Barrel of Ilmenau (BOI) with the cylindrical experimental cell of 7 m in diameter and variable height of up to 6.3 m represents the worldwide largest experimental setup to study highly turbulent RBC using dry air as a working fluid. The BOI is newly equipped with the LUNA ODISI B system for temperature profiles measurements. The system permits to measure the temperature and its fluctuations with high spatial resolution of 5 mm along a very thin glass optical fibre with the length of 5 m, and high acquisition rate up to 100 Hz. The content of this work is to perform measurements of vertical temperature profiles and fluctuations along the axis of the cell (and another suitably chosen radial position near to the sidewall) with the height of 4.7 m. The results should lead to better understanding of the structure and dynamics of the layers adjacent to the plates (boundary layers), which are limiting the global heat transport in the RBC system.

Master's Thesis goals:

1. Get familiar with the Barrel of Ilmenau experimental facility as well as with the LUNA ODISI-B optical fibre measurement system, perform the test measurements.
2. Measure the temperature profiles and temperature fluctuations measurements for various intensities of turbulence in RBC.
3. Process and evaluate the measured data and interpret the results.

Recommended bibliography:

CHILLA, F., SCHUMACHER, J., New perspectives in turbulent Rayleigh-Benard convection, European Physics Journal E, 35, p. 58, 2012.

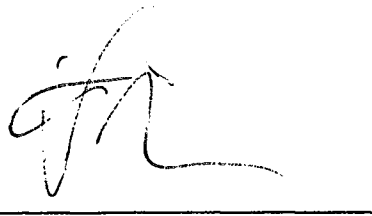
URBAN, P., SKRBK, L., Has the ultimate state of turbulent thermal convection been observed?, J. Fluid Mech. 785, pp. 270-282, 2015.

MUSILOVÁ, V., KRÁLIK, T., La MANTIA, M., MACEK, M., URBAN, P., SKRBK, L., Reynolds number scaling in cryogenic turbulent Rayleigh-Bénard convection in a cylindrical aspect ratio one cell, J. Fluid Mech. 832, pp. 721-744, 2017.

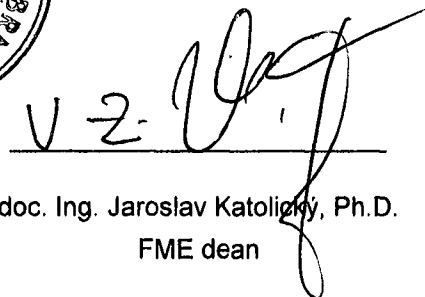
TRITTON, D. J., Physical fluid dynamics. 2nd edition. Oxford: Clarendon Press, 1988.

Students are required to submit the thesis within the deadlines stated in the schedule of the academic year 2017/18.

In Brno, 3. 11. 2017



prof. RNDr. Tomáš Šikola, CSc.
Director of the Institute



doc. Ing. Jaroslav Katolický, Ph.D.
FME dean

ABSTRACT

This work describes experimental research directed at the study of vertical temperature profiles and fluctuations in the turbulent Rayleigh-Bénard convection. Experiments took place in Barrel of Ilmenau containing the cylindrical experimental cell with a diameter of 7.15 m and the height of 4.70 m (the aspect ratio $\Gamma = 1.5$) filled with dry air. The temperature profiles and fluctuations were studied along the vertical axis of the cell between the top and bottom plates within the range of Rayleigh number (Ra) of $1 \times 10^{11} - 4 \times 10^{12}$. The temperature profiles were measured by a novel method using the optical fibre system Luna ODiSI-B which was purchased by the team in Ilmenau. The system permits to measure the temperature profile simultaneously along the whole optical fibre length with a spatial resolution of 5 mm.

KEYWORDS

Rayleigh-Bénard convection, Barrel of Ilmenau, temperature profiles, temperature fluctuations, Luna ODiSI-B, Optical Distributed Sensor Interrogator

ABSTRAKT

Tato práce popisuje výzkum zaměřený na studium vertikálních teplotních profilů a fluktuací v turbulentní Rayleighově-Bénardově konvekci. Experiment byl proveden v „Barrel of Ilmenau“ obsahující válcovou experimentální celu s průměrem 7.15 m a výškou 4.7 m („the aspect ratio“ $\Gamma = 1.5$) naplněnou suchým vzduchem. Teplotní profily a fluktuace byly studovány podél vertikální osy cely mezi horní a spodní deskou v rozmezí Rayleighova čísla (Ra) $1 \times 10^{11} - 4 \times 10^{12}$. Teplotní profily byly změřeny novou metodou využívající systém s optickým vláknem Luna ODiSI-B, který byl pořízen týmem z Ilmenau. Systém umožňuje měřit teplotní profil ve všech bodech podél celého vlákna současně s prostorovým rozlišením 5 mm.

KLÍČOVÁ SLOVA

Rayleigh-Bénardova konvekce, Barrel of Ilmenau, teplotní profily, teplotní fluktuace, Luna ODiSI-B, Optical Distributed Sensor Interrogator

DRAHOTSKÝ, Jakub *Temperature profiles and temperature fluctuations in turbulent Rayleigh-Bénard convection*: master's thesis. Brno: Brno University of Technology, Faculty of Mechanical Engineering, Institute of Physical Engineering, 2018. 69 p. Supervised by Ing. Pavel Urban, Ph.D.

DECLARATION

I declare that I have elaborated my master's thesis on the theme of "Temperature profiles and temperature fluctuations in turbulent Rayleigh-Bénard convection" independently, under the supervision of the master's thesis supervisor and with the use of technical literature and other sources of information which are all quoted in the thesis and detailed in the list of literature at the end of the thesis.

As the author of the master's thesis I furthermore declare that, concerning the creation of this master's thesis, master's thesis, I have not infringed any copyright. In particular, I have not unlawfully encroached on anyone's personal copyright and I am fully aware of the consequences in the case of breaking Regulation §11 and the following of the Copyright Act No 121/2000 Vol., including the possible consequences of criminal law resulted from Regulation § 152 of Criminal Act No 140/1961 Vol.

Brno

.....

(author's signature)

Acknowledgements

I would first like to thank my supervisor Dr. Pavel Urban and Dr. Ronald du Puits for leadership during my Erasmus stay. I would like to also thank to my colleagues from Institute of Scientific Instruments for stimulating discussions - Dr. Věra Musilová, Dr. Michal Macek, Pavel Hanzelka, Dr. Tomáš Králík, Dr. Jiří Frolec. The fibre installation into the cell and planned experiments were realised with the valuable assistance of the technical staff in Ilmenau - Sabine Abawi and Vigimantas Mitschunas.

I acknowledge the support of the experimental part of this research by the European Community Framework Programme 7, EuHIT (European Highperformance Infrastructures in Turbulence) Grant Agreement No. 312778. The data were evaluated with the support of the Czech Science Foundation under the project GA17-03572S and the MEYS CR project LO1212.

Jakub Drahotský

CONTENTS

Introduction	1
1 Theory	5
1.1 Equations describing RBC	5
1.2 Dimensionless quantities for description of RBC	6
1.3 Temperatures profiles in RBC	8
1.4 Non-Oberbeck-Boussinesq effects	10
2 Experimental arrangement	13
2.1 Barrel of Ilmenau	13
2.2 Luna ODiSI-B	14
2.2.1 Rayleigh scattering	16
2.2.2 Coherent optical frequency domain reflectometry	17
2.3 Pt100 probes	18
2.4 Experimental arrangement	18
3 Results and discussion	23
3.1 Properties of air around measurement point	26
3.2 Core temperature measurements	28
3.3 Temperature profiles	31
3.3.1 Temperature profiles by Pt100 probes	31
3.3.2 Frequency shift and taring	39
3.3.3 Calibration	44
3.3.4 Temperature profiles by ODiSI-B	46
3.4 Fluctuations and coherent structures	47
3.4.1 Detrended frequency shift	47
3.4.2 Autocorrelation and crosscorrelation	50
3.4.3 Characteristics of coherent structures	57
4 Summary and conclusions	59
Bibliography	61
List of symbols, physical constants and abbreviations	67

INTRODUCTION

Natural thermally-generated turbulent convection plays a vital role in heat and mass transfer in nature, such as the circulation in the atmosphere or the oceans, the flows under the surface of stars or in diverse branches of industry. Modelling of large-scale natural convection in laboratory experiments is possible on the base of a simplified physical model system called the Rayleigh-Bénard convection (RBC). Turbulent RBC is often realized in a layer of working fluid confined to a cylindrical experimental cell which is heated from the bottom and cooled from above with a vertical temperature gradient parallel to gravity. Since RBC is wall-bounded flow, boundary layers of both the temperature and velocity fields form at the upper and bottom isothermal plates due to finite viscosity. [1]

The structure and dynamics of the temperature boundary layers (BLs) turn out to be crucial for a deeper understanding of the global heat transport process in RBC as discussed for example in a recent review [2–4]. The global heat transport in turbulent RBC is characterised by the dimensionless Nusselt number Nu which is function of the three dimensionless control parameters: the Rayleigh number Ra , the Prandtl number Pr and the aspect ratio Γ of the convection cell, i.e. $Nu = Nu(Ra, Pr, \Gamma)$. Various theories yield different predictions of $Nu(Ra, Pr, \Gamma)$ scaling based on a different assumption on the BLs structure [3].

On the other hand, the structure and dynamics of the BLs are influenced by interaction with a so-called large-scale circulation (LSC) that is always established in the turbulent bulk of RBC (see fig. 1). The LSC take the form of a single roll for Γ of order unity or multiple rolls for larger aspect ratios Γ [6]. The complex three-dimensional dynamics of LSC (its irregular cessations, reversals, azimuthal meandering and periodical sloshing and twisting modes, see fig. 2) and the interplay between LSC and BLs are still insufficiently understand. It is supposed that LSC is triggered by packets of thermal plumes, fragments of the thermal BLs, which are detached randomly from both layers into the bulk of RBC (fig. 1). These organized coherent structures, plumes and LSC, can be characterized by suitably defined dimensionless Reynolds numbers Re [7].

Interaction of the LSC with the boundary layers likely leads to the laminar-to-turbulent transition in the boundary layers, which is presumably related to the transition to the ultimate regime of RBC with ballistic heat transport idea, predicted theoretically by Kraichnan [8]. Confirmation of such transition would also be of great practical importance, as the heat transport efficiency rises significantly (from $Nu \sim Ra^{1/3}$ to $Nu \sim Ra^{1/2}$). Detailed study of thermal BLs at high Ra numbers (at $Ra > 10^9$) requires large devices such as the Barrel of Ilmenau (BOI), because their thickness λ_T decreases as the Ra and thus the Nu number grow.

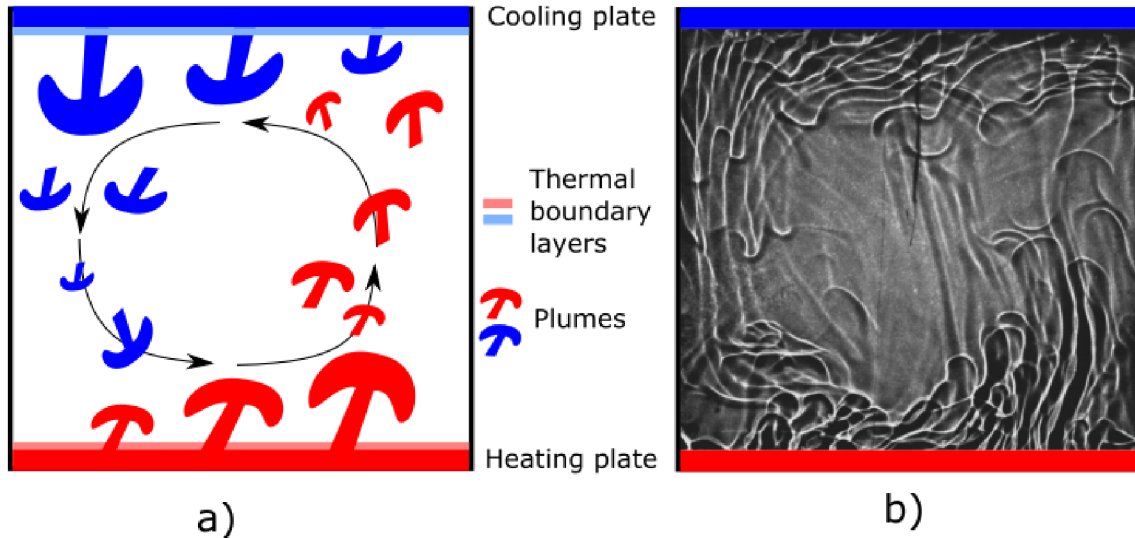


Fig. 1: a) Representation of the fluid movements in the RBC experiment. The fluid is heated up at the heating plate, decrease its density and in structures called plumes is moving up. At the cooling plate, the fluid is cooled down and reversing its direction to the heating plate. The main trend of the movements is shown as large-scale wind direction. Biggest temperature changes are happening at the thin layers of fluid near the plates called boundary layers (BL). b) Experimental image of the glycerol in the RBC experiment. Plumes are clearly visible. The black line from the middle of the cooling plate is temperature probe. Adapted from [5].

The thickness is given by $\lambda_T = L/2Nu$, where L is the height of the cell (for $Ra \sim 10^9$, $L = 4.7\text{m}$: $\lambda_T \sim 1\text{cm}$). Simultaneously, high-resolution techniques for temperature measurement in the thermal BLs are necessary for such study.

This work was created within the collaboration of Institute of Scientific Instruments of the CAS (ISI CAS) and Ilmenau University of Technology (TU Ilmenau). The main impulse for this collaboration was created by European High-Performance Infrastructures in Turbulence (EuHIT) that aims at integrating cutting-edge European facilities or turbulence research. Since both facilities - Brno and Ilmenau are part of this project, EuHIT partly financed the investigation time in Ilmenau, the second part was financed by Erasmus+.

The principal motivation for the EuHIT project [9] was to shed light on discrepancies among published results on Rayleigh-Bénard convection (RBC) around Ra number 10^{11} in $Nu(Ra, Pr, \Gamma)$ and $Re(Ra, Pr, \Gamma)$ scaling laws and influence of Non-Oberbeck-Boussinesq (NOB) effects on RBC (see chapter 1.4), especially on a possible transition of RBC to the ultimate (Kraichnan) regime. It was observed experimentally that NOB effects do indeed lead to asymmetry of the boundary layers, which subsequently alters the heat transfer efficiency at high Ra . To appreciate NOB

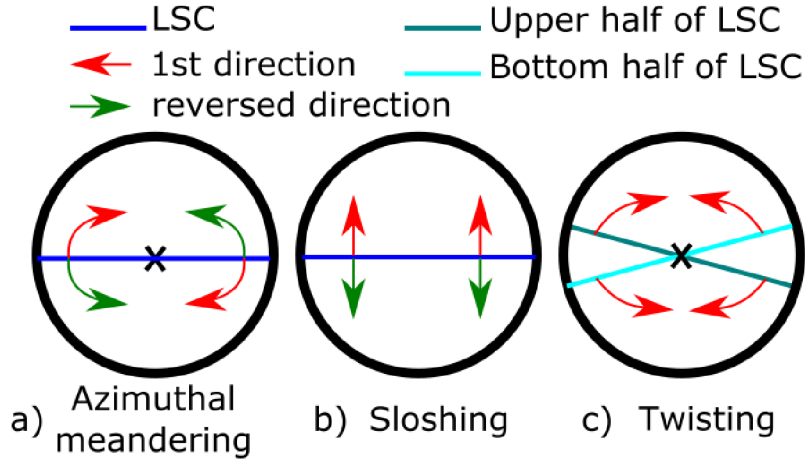


Fig. 2: Possible movements of the LSC in the cell from top view. a) Azimuthal meandering of the LSC around the central axis of the cell is uniform movement of the plane in which is the wind located. This movement is random and thus without a period. b) Sloshing is deflection of the plane of the wind to some side in the horizontal direction. c) Twisting is a fluent movement of the LSC, where part located at top plate are moving in opposite direction than the part located at bottom plate - LSC plane is twisted. Only one direction of the move is shown in the picture. Sloshing and twisting are both periodic movements that can be described by period of the move.

effects we focused on measurement of the vertical temperature profiles in Oberbeck-Boussinesq (OB) and NOB case of room temperature air across the cylindrical cell with aspect ratio $\Gamma \sim 1$.

The experiment took place in the Barrel of Ilmenau (at TU Ilmenau) which is newly equipped with a technique using the fibre-optic temperature measurement system Luna ODiSI-B (Optical Distributed Sensor Interrogator) for temperature profiles measurements. The system permits to measure the temperatures along a very thin glass fibre and seemed to be perfectly suited to measure vertical profiles in the Barrel of Ilmenau. The temperature profile in RBC has not yet been measured along the full cell height instantaneously and with such high spatial resolution in any laboratory. The optical fibre system was a completely new equipment at the BOI and both our team and the staff in Ilmenau had no former experience with this method of temperature measurement. Thus to get the apparatus simply running was a major experimental challenge. This was accomplished in relatively short time. The system was supplemented with the two Pt100 vertically movable probes specially designed by us for reference temperature profiles measurements. Opposite to Pt100 probes, the Luna ODiSI-B is promising for the study of the time-dependence [10] of temperature profiles and space-time temperature correlations [7].

The first part of measurement was done in the period from the 12th February 2017 until the 31st March 2017. Then the data was evaluated and the measurement setup was improved.. The rest of the measurements was done in the period from the 9th June 2017 until the 18th July 2017. Data were afterwards processed in Brno. The primary goal of the EuHIT project is to advance the competitiveness of the European turbulence research with special focus on providing the shared knowledge or technological innovation. For this reason, all data measured during any EuHIT project are collected in a freely accessible database TurBase [11]. In this work, we will publish only representative results. All our findings and data will be published in this database, including the Matlab scripts that were created during this work. Part of the results will appear in the publication [12].

The thesis is organized as follows. In chapter 1, equations describing RBC as well as non-dimensional parameters for evaluation of RBC are introduced. Experimental apparatus and both techniques, using Luna ODiSI-B and Pt100 probes, are presented in chapter 2. In chapter 3, we present the experimental data obtained and discuss them in comparison with available data from other experiments. Conclusions are given in chapter 4.

1 THEORY

1.1 Equations describing RBC

The motion of incompressible Newtonian fluid in gravitational field can be described by Navier-Stokes (NS) equations:

$$\underbrace{\rho \left(\frac{\partial \mathbf{u}}{\partial t} + (\mathbf{u} \cdot \nabla) \mathbf{u} \right)}_{\text{inertial forces}} = \underbrace{-\nabla p}_{\text{pressure forces}} + \underbrace{\mu \nabla^2 \mathbf{u}}_{\text{viscous forces}} + \underbrace{\rho \mathbf{g}}_{\text{buoyancy forces}}, \quad (1.1)$$

where \mathbf{u} is the flow velocity, t is the time, ρ is the fluid density, p is the fluid pressure, μ is the dynamic viscosity, \mathbf{g} represents the gravitational acceleration. These equations represent conservation of momentum in the system.

By employing the OB approximation, we can rewrite the buoyancy term as $(\rho_0 + \Delta\rho)\mathbf{g}$, where $\Delta\rho$ is representing the density variations from ρ_0 . Since we want to avoid evaluation of this term based on local density, for small temperature differences, we can further write $\Delta\rho\mathbf{g} = -\rho_0\alpha\Delta T\mathbf{g}$, where α is the coefficient of thermal expansion and ΔT is the temperature difference between plates. NS equations can thus be rewritten as

$$\rho_0 \left(\frac{\partial \mathbf{u}}{\partial t} + (\mathbf{u} \cdot \nabla) \mathbf{u} \right) = -\nabla p + \mu \nabla^2 \mathbf{u} + \rho_0 \mathbf{g} - \rho_0 \alpha \Delta T \mathbf{g}, \quad (1.2)$$

To further simplify the situation, the so called "pressure shift" [13] is introduced into the buoyancy term as $P = p + \rho_0 g H$, where H is the elevation. $-\nabla p + \rho_0 \mathbf{g}$ can be rewritten as $-\nabla P$. After dividing by ρ_0 we get:

$$\frac{\partial \mathbf{u}}{\partial t} + (\mathbf{u} \cdot \nabla) \mathbf{u} = -\frac{1}{\rho_0} \nabla P + \nu \nabla^2 \mathbf{u} - \alpha \Delta T \mathbf{g}, \quad (1.3)$$

where $\nu = \mu/\rho_0$ is the kinematic viscosity.

The NS equations are always solved together with the continuity equation (1.4), which represents the conservation of mass.

$$\frac{\partial \rho}{\partial t} + \nabla \cdot (\rho \mathbf{u}) = 0 \quad (1.4)$$

Under the OB approximation, the equation reduces to the incompressible form

$$\nabla \cdot \mathbf{u} = 0. \quad (1.5)$$

Since the motion in the system is caused by heat exchange, the equation of energy conservation is expressed as:

$$\frac{\partial T}{\partial t} + \mathbf{u} \cdot \nabla T = \kappa \nabla^2 T, \quad (1.6)$$

where κ is the thermal diffusivity. Equations 1.3, 1.5, 1.6 now represents the OB system of equations for describing of OB RBC.

It is important to highlight that the OB approximation is not valid in case of violation any of these conditions:

- Properties of fluid $\mu, \alpha, \nu, \kappa, \lambda, h$ are constant with temperature.
- Continuity equation is expressed in incompressible form.
- Density ρ in the buoyancy term is dependent on temperature as $\rho = \rho_0(1 - \alpha T)$, i.e. linearly.

1.2 Dimensionless quantities for description of RBC

To derive the non-dimensional NS equations, several appropriate scales must be introduced to the system. These are listed in the table 1.1.

Tab. 1.1: Scales for non-dimensionalization of equations 1.3 and 1.6. It can be shown, that free fall velocity $U = \sqrt{g\alpha L\Delta T}$.

Characteristic scale	Dimensionless variable
Length L	$\mathbf{r}^* = \frac{\mathbf{r}}{L}, \nabla^* = L\nabla$
Flow velocity U	$\mathbf{u}^* = \frac{\mathbf{u}}{U}$
Time $T = L/U$	$t^* = \frac{t}{T} = \frac{tU}{L}$
Pressure $P/$	$P^* = \frac{P}{\rho_0 U^2}$
Gravitational acceleration vector \mathbf{g}	$\mathbf{z}^* = \frac{\mathbf{g}}{ \mathbf{g} }$

Neglect the last buoyancy term in equation 1.3 for a while. The NS equations becomes

$$\frac{\partial \mathbf{u}^*}{\partial t^*} + (\mathbf{u}^* \cdot \nabla^*) \mathbf{u}^* = -\nabla^* P^* + \frac{1}{Re} \nabla^{*2} \mathbf{u}^*, \quad (1.7)$$

where Re is **Reynolds number**, which quantifies if the viscous or inertial forces are dominant in the flow. Low $Re \sim 1000$ numbers are associated with laminar flows, higher Re numbers are connected with turbulent flows with highly random eddies and vortices. The structure of the turbulence should be very similar for systems with same Re number, regardless of the size of a system.

When we account for the buoyancy term, we can derive the nondimensionalized equations describing the RBC under the Boussinesq approximation from equations 1.3, 1.5, 1.6 as:

$$\frac{\partial \mathbf{u}^*}{\partial t^*} + (\mathbf{u}^* \cdot \nabla^*) \mathbf{u}^* = -\nabla^* P^* + \sqrt{\frac{Pr}{Ra}} \nabla^{*2} \mathbf{u}^* - \Delta T \mathbf{z}^*, \quad (1.8)$$

$$\frac{\partial T^*}{\partial t^*} + \mathbf{u}^* \cdot \nabla^* T^* = \sqrt{\frac{1}{Pr \cdot Ra}} \nabla^{*2} T^*, \quad (1.9)$$

$$\nabla^* \cdot \mathbf{u}^* = 0, \quad (1.10)$$

where Ra is the **Rayleigh number** and Pr is the **Prandtl number** [14].

Rayleigh number is primarily connected with buoyancy flows. When $Ra < 1078$, heat transfer in the system is by conduction. If Ra exceeds the critical value, heat transfer is mainly due to convection.

Prandtl number is the ratio of momentum diffusivity to thermal diffusivity. At small **Prandtl numbers** $Pr \ll 1$ the thermal diffusivity dominates. At higher Pr numbers the momentum diffusivity dominates.

Heat transfer efficiency is characterized by **Nusselt number** $Nu = \frac{hL}{\lambda}$, where h is the convective heat transfer coefficient of the flow and λ is the thermal conductivity of the fluid. Nusselt number measures the ratio between heat transfer by convection and conduction.

In reality, the experiments are often conducted in a cylindrical cell with a finite diameter of the plates. The wall restrictions for the LSC - the boundary condition are expressed by **aspect ratio** $\Gamma = D/L$, where D is the diameter of the cell.

Tab. 1.2: Overview of dimensionless numbers used in RBC.

Dimensionless number	Mathematical definition	Description
Reynolds number	$Re = \frac{UL}{\nu}$	Ratio of advection to diffusion effects
Rayleigh number	$Ra = \frac{g\alpha\Delta TL^3}{\nu\kappa}$	Ratio of buoyancy to viscosity forces
Prandtl number	$Pr = \frac{\nu}{\kappa}$	Ratio of viscous to thermal diffusion rates
Nusselt number	$Nu = \frac{hL}{\lambda}$	Ratio of convective to conductive heat flux
Aspect ratio	$\Gamma = D/L$	Geometrical parameter of the cell

1.3 Temperatures profiles in RBC

Very simple model of temperature profiles in RBC is proposed in [14]. For a non-dimensional system for which bottom and top plates are separated by unit distance and are kept at temperatures 1 at the heating plate and 0 at the cooling plate, we define planar average temperature $T_p(z) = \langle T \rangle_{xy}$, where $\langle \cdot \rangle_{xy}$ denotes an average over a plane at fixed height z . By experimental observations, $T_p(z) \sim 1/2$ in the core region, and it drops abruptly in the boundary layers. $T_p(z)$ can be approximated as

$$T_p(z) = \begin{cases} 1 - \frac{z}{2\lambda_T}, & \text{if } 0 < z < \lambda_T, \\ 1/2, & \text{if } \lambda_T < z < 1 - \lambda_T, \\ \frac{1-z}{2\lambda_T}, & \text{if } 1 - \lambda_T < z < 1, \end{cases} \quad (1.11)$$

where λ_T is the thickness of the thermal boundary layer.

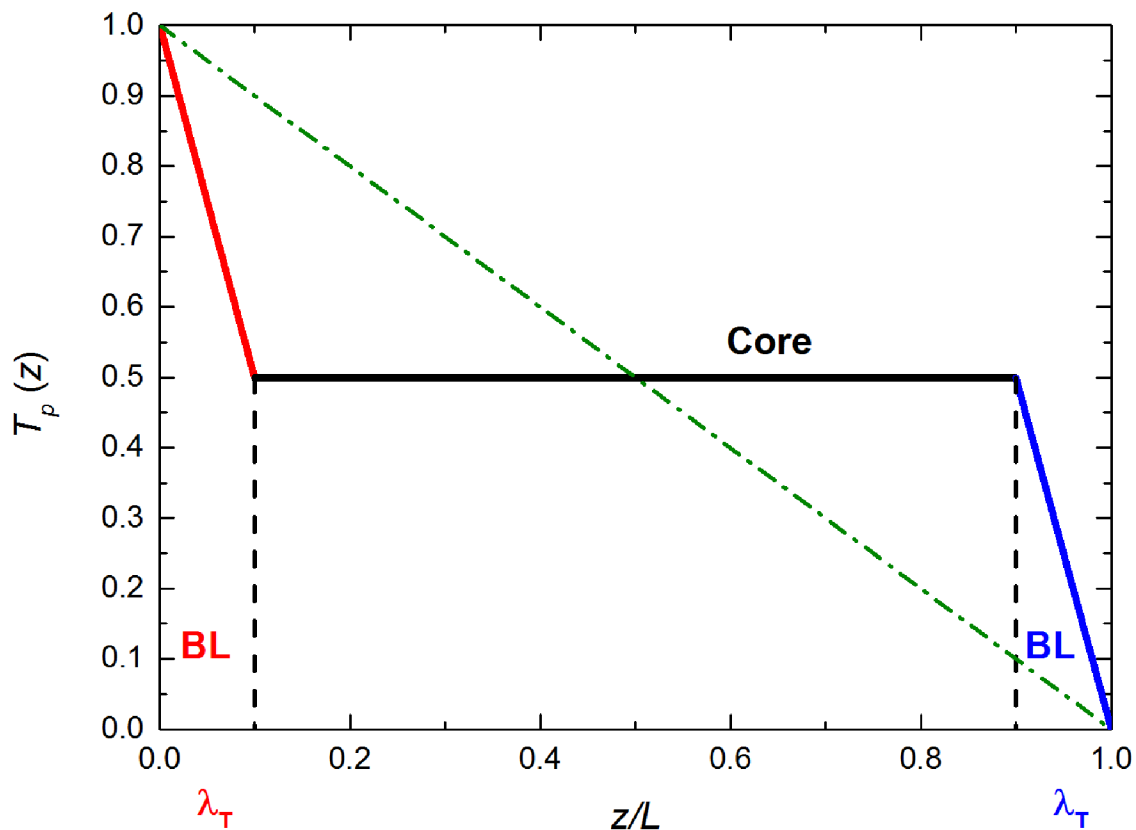


Fig. 1.1: A schematic diagram of the planar-averaged convection temperature profile $T_p(z)$ as a function of the vertical non-dimensional coordinate z/L . The temperature drops sharply to 1/2 in the boundary layers. Green dash-dot line shows a conduction profile. Adapted from [14].

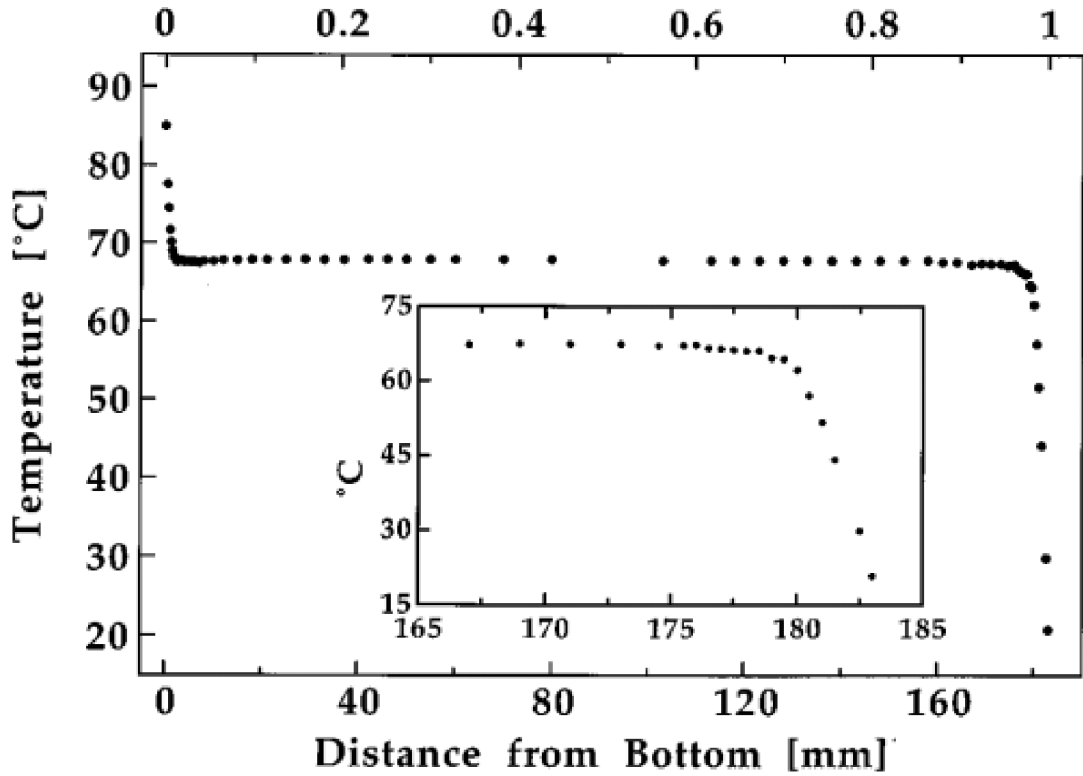


Fig. 1.2: Experimentally measured time-averaged temperature profile in glycerol as a function of distance from the heating plate. The profile was measured at the temperature of the top cooling plate $T_t = 15^\circ\text{C}$, temperature of the bottom heating plate $T_b = 94^\circ\text{C}$ and mean temperature $T_m = 54.5^\circ\text{C}$. The cell was cubic box with a characteristic length $L = 183\text{ cm}$. Enlarged portion of the profile near the top plate is in the inset. Every point was measured 20 min with sampling rate 5 Hz. Upper scale is normalized distance z/L based on the length of the cell. $Ra = 6.1 \times 10^8$, $Pr = 500$. [5]

The experimentally measured temperature profile (of vertical central axis) in the glycerol is in the fig. 1.2. It can be seen, that temperature change in boundary layers is very quick and not as sharp as in the fig. 1.1. Very significant is that the core temperature T_c is higher than the mean temperature $T_m = (T_b + T_t)/2$, where T_b is the temperature of the heating plate and T_t is the temperature of the cooling plate. This shift is due to NOB effects described in the next chapter.

1.4 Non-Oberbeck-Boussinesq effects

OB approximation was already introduced in chapter 1.1. In experiments, this approximation is assumed to be valid when the temperature variation of the density ρ is less than a few percent and deviations of other fluid properties are very small. In this case of OB RBC, the temperature drops on the top and bottom thermal boundary layers are equal and turbulent core temperature T_c is equal to the mean temperature T_m (see fig. 1.3 a). Temperature drops at the boundary layers can be defined as $\Delta_{OB} \equiv T_b - T_m = T_m - T_t$. [15]

One of the experimentally observed effects at large temperature differences ΔT is that temperature drop across the top $\Delta_t = T_b - T_c$ and the bottom $\Delta_b = T_c - T_t$ thermal boundary layers become asymmetric. The asymmetry between boundary layers naturally also shift core temperature from $T_m = 1/2$ on a non-dimensional scale to slightly different value T_c (fig. 1.3 b). This deviation is due to Non-Oberbeck-Boussinesq effects.

The comparison of vertical temperature profiles for OB and NOB RBC cases are presented in fig. 1.3 c). The vertical thickness of the bottom BL is λ_b and the vertical thickness of top BL is λ_t . From experiments [5, 15–17] we can observe that T_c can be both higher or lower than T_m .

According to [16], the NOB effects significantly influence laminar boundary layers and can be well described by an extension of the Prandtl-Blasius boundary layer theory [18]. Authors point out that for most of published experiments [5, 15–17, 19], the parameter of asymmetry $\chi \equiv \Delta_t/\Delta_b$ is higher than 1 for liquids and lower than 1 for gases. In most publications, χ has an increasing or decreasing trend with the higher temperature difference between the plates. The authors give this explanation: in liquids $(\partial\mu/\partial T)_\rho < 0$, where μ is the dynamic viscosity and ρ density, leads to a thinner thermal BL between the centre and the hot bottom plate, implying an enhanced centre temperature. For gases, however, the bottom viscous BL expands due to the temperature dependence of the density, inducing also an extension of the thermal BL between the hot bottom and the centre, thus implying a larger temperature drop across that BL, i.e., a reduced centre temperature T_c .

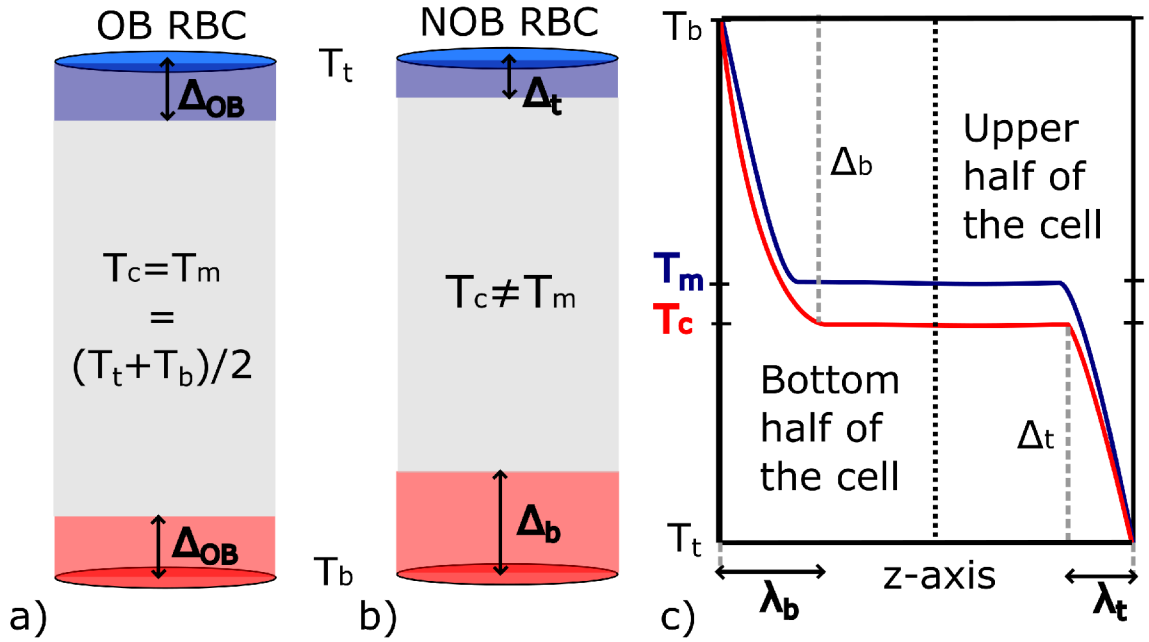


Fig. 1.3: Schematic illustration of the thermal boundary layers and vertical temperature profiles in RBC: a) Thermal boundary layers in OB RBC where the temperature drops Δ_{OB} on the top and bottom boundary layers are equal. The turbulent core temperature T_c equals the mean temperature T_m . b) Thermal boundary layers in NOB RBC, where the temperature drops on the top ($\Delta_t = T_c - T_t$) and bottom ($\Delta_b = T_b - T_c$) layers are asymmetric. The turbulent core temperature T_c differs from the mean temperature T_m . c) The vertical temperature profile in the OB (blue) and NOB (red) RBC. λ_t and λ_b represents the thickness of the top and bottom boundary layers.

2 EXPERIMENTAL ARRANGEMENT

2.1 Barrel of Ilmenau

Barrel of Ilmenau (fig. 2.1) is a worldwide largest experimental facility for studying highly turbulent convection using dry air as a working fluid. The facility is located in the Ilmenau, Germany and operated by the Ilmenau University of Technology. [20]



Fig. 2.1: Experimental facility Barrel of Ilmenau is a worldwide largest experiment for the study of highly turbulent convection in dry air. Diameter $D = 7.15$ m, height L can be adjusted up to 6.3 m).

The arrangement of the experimental cell in BOI is illustrated in fig. 2.2. Closed cylindrical cell (F, K) is filled with dry air (N). The free-hanging vertically movable cooling plate (A) allows adjusting the distance from the bottom plate from 0.2 to 6.3 m. It is created from water-cooled aluminium plates made of 16 separate segments each covering a sector of angle 22.5° . The accuracy of the temperature set at the plate is better than $\pm 0.1^\circ\text{C}$ [6]. The bottom heating is composed of four layers (C, D, E and overlay). The isolation is created by electrical underfloor heating system (D) in a 5 cm concrete layer (C) which is isolated to the ground by 0.3 m polyurethane plates (E). At the top is an overlay (which is not shown in the figure) above C layer in which circulates a water. The temperature deviations of the hot plate are typically less than $\pm 1\%$ of the total temperature drop between the plates. At cooling plate, the deviations are $\pm 1.5\%$. The perpendicularity of the plates alignment is lower than 0.1° . The volume of the cell at $\Gamma = 1.13$ is about 250 m. Technical data of the Barrel are summarized in the table 2.1. For more detail information see [21, 22].

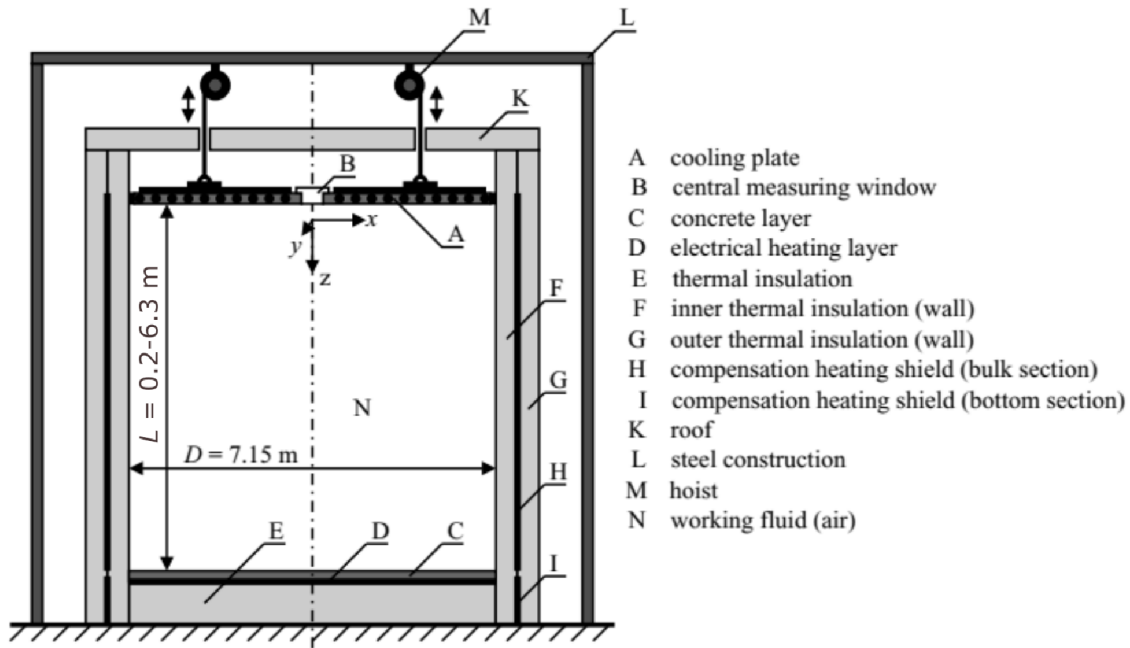


Fig. 2.2: Experimental cell of the BOI. [6]

Tab. 2.1: Technical data and physical parameters of the Barrel of Ilmenau. [20]

Diameter D	7.15 m
Adjustable height L	0.2...6.3 m
Temperature of the heating plate T_b	10...80 °C
Temperature of the cooling plate T_t	10...80 °C
Sidewall	no heat flux
Working fluid	dry air
Rayleigh number Ra	$10^5 \dots 10^{12}$
Aspect ratio Γ	1.13...40
Prandtl number Pr	0.7
Nusselt number Nu	...650
Reynolds number Re	$\dots 3 \times 10^5$

2.2 Luna ODiSI-B

Luna ODiSI-B is a system that uses a thin glass optical fibre as a sensor for distributed temperature or strain measurements based on Rayleigh scattering, evaluated by coherent Optical Frequency Domain Reflectometry (c-OFDR) combined with a Mach Zehnder interferometer [23]. The resulting quantity indicated by the system is called the “frequency shift” that is converted into a temperature information by a suitable calibration (see sec. 3.3.3). In general, the system permits to measure the

temperature profiles along the fibre with the length of up to 20 m with an acquisition rate of 250 Hz and spatial resolution down to 1.25 mm in dependence on the type of the system configuration. Detailed parameters of the system used in our experiments are given in table 2.2.

The device itself consists mainly of a tunable laser with central wavelength 1546 nm that can be tuned over a range of 60 nm [24], fibre-based Mach-Zehnder interferometer, two polarization sensitive detector and optical fibre sensor placed in the area of interest [23]. The arrangement of the individual components of ODiSI-B is shown in the fig. 2.3. The light from the continually tunable laser is split by the optical coupler to the two legs of the optical interferometer. The light in the upper measurement leg is guided by delay cable to the fibre sensor which is placed in the area of interest. The strain and temperature differences acting on fibre sensor alters the refractive index of the lattice structure – causes a spectral shift in Rayleigh backscattering which passes through the same cable back to the delay cable and next coupler as is indicated by arrows [25]. There it meets with light from bottom reference leg. The interference light is detected by two polarization sensitive detectors (P, S). Fast Fourier transform (FFT) analysis of the beat frequency of interferometer legs allows to visualize multiple reflections at once and determined their locations. The detected Rayleigh spectra for a specific location is then compared to the one measured at stable conditions. Frequency shifts of Rayleigh spectra at individual locations are computed by crosscorrelation. With correct calibration, frequency shift can be converted to relative temperature or strain. The key technologies that are utilized in this device will be explained in more detail in next sections.

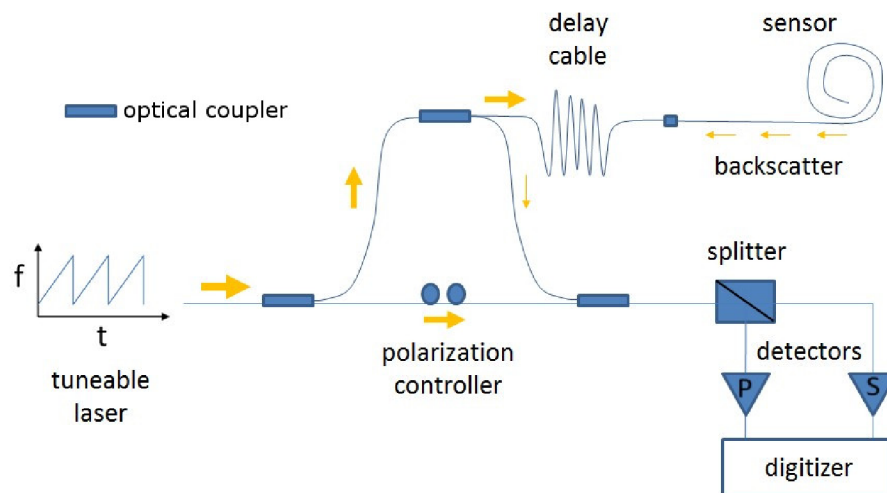


Fig. 2.3: Scheme of the main components of the ODiSI-B. [26]

Tab. 2.2: Specification of ODiSI-B used in our experiment from datasheet [27].

Maximum sensor length	10 m
Spatial resolution	5.2 mm
Measurement temperature range	-40...220°C
Temperature resolution	< 0.1 °C
Temperature repeatability	±0.01 °C
Data acquisition rate	up to 100 Hz

2.2.1 Rayleigh scattering

For many years, fibre sensors are used for temperatures or strain measurements in environments where electrical sensors could not be applicable. This involves applications with large electromagnetic field or hazardous environments. Fibre sensors compared to classical point temperature/strain sensors allows to measure properties along a large distance (to several km) with high spatial resolution (to few mm). For a long time, the sensing was provided either by Brillouin or Raman scattering. In last decade, the advantage of Rayleigh scattering with the c-OFDR technique starts to be used. Very high performance was reported with this technique: a temperature resolution 0.1 °C and spatial resolution of 2 mm [28].

Rayleigh scattering of light occurs at particles and inhomogeneities much smaller than the wavelength of the light and can happen at individual atoms and molecules. The amplitude of scattered light is proportional to the incoming light amplitude like fourth power of the inverse wavelength $I_{scattered} \sim 1/\lambda^4$. Scattering under the angle is described by $1 + \cos\theta$, where θ is the scattering angle. From this relation, we can see that forward and backward scattering ($\phi = 0$ and $\phi = \pi$, respectively) are equally strong. [29]

For fibre sensing, mostly the silica glass fibres are used. Since this material is amorphous, it contains random density perturbations in irregular microscopic structure. The Rayleigh scattering takes advantage of this inhomogeneities and thus no special modification of the fibre is needed.

In the measurement system, Rayleigh-based scattering is used only to track propagations effects of fibre sensor, which provide the real sensing mechanism. Such effects can contain attenuation, gain, interference and polarization variation. This phenomenon is the reason of main disadvantage of Rayleigh scattering over other scattering techniques. Rayleigh signal is sensitive to many different physical fields - besides temperature and strain also to humidity, microbending effects, pressure and concentration of chemicals. In the measurement setup, it is very difficult to dampen all others contributors and observe only one of interest. [30]

2.2.2 Coherent optical frequency domain reflectometry

C-OFDR technique is based on the detection of a beat signal between the distributed reflections from the fibre under the test (caused by Rayleigh backscatter, connectors, etc.) and fixed Fresnel reflection (from local oscillator). Scheme of this technique is in fig. 2.4. Linear frequency swept of the laser light allows to directly measure beat frequencies on a distance scale. At the same time, normed square power for a given beat frequency gives the reflectivity (and after calibration any other dependent quantity) at the corresponding distance. In ODiSI-B was local oscillator replaced by Mach-Zehnder interferometer. [31]

The measurement range of the c-OFDR is limited especially by the coherent length of the laser due to signal fading and phase noise as it reduces dynamic range. The spatial resolution along the fibre is limited by frequency excursion of the laser, measurement range and number of points used. [31]

More about c-OFDR can be found in [32–34].

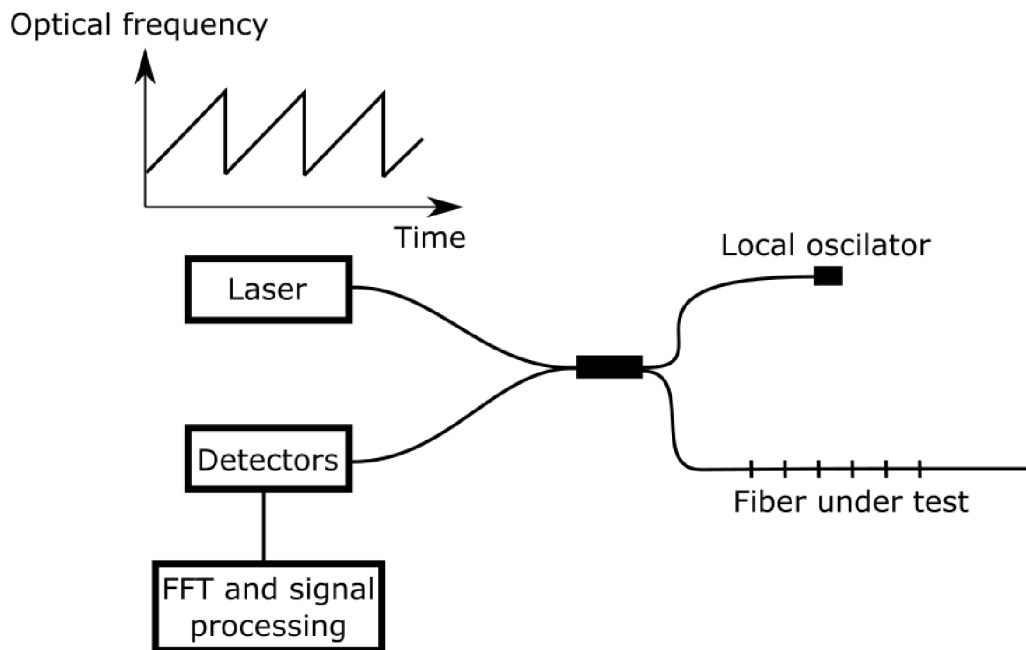


Fig. 2.4: Schematic set-up of the c-OFDR. Adapted from [31].

2.3 Pt100 probes

Since ODiSI-B is capable to measure only relative temperatures, it was necessary to measure also the absolute temperature at some known location along the fibre. For this purpose, two Pt100 probes were prepared at Institute of Scientific Instruments of the CAS (ISI). One probe was used for measuring in the region of bottom BL and turbulent core. The second probe measured mainly in the region of top BL: up to 30 cm below the cooling plate. Both probes were suspended on the feed cables passing through the hole in the top plate and could be moved by hand via cables up and down in parallel to the optical sensor.

Both probes are identical and their photo is in fig. 2.5. From the left of the figure, both probes start with the gold tip for electrical contact with a copper plate that was placed beneath the sensors on the surface of the heating plate. This closed circuit served as "touch" indicator because on 5 m distance was very difficult to determine when the sensor is in contact with a heating plate. Above the tips on the golden plate are placed Pt100 sensors in a horizontal position to lower the cross-section of the sensors in the vertical direction. Pt100s were class A, produced by ZPA EKOREG s.r.o., type 03 002 [35]. As the support elements, fibreglass rods with a very low thermal conductivity were used. Phosphor bronze quad-lead wires from Pt100 to cable connectors were purchased from Lakeshore, type WQL 36. To prevent swinging caused by the 5 m cable, we placed two guide handles to the fibreglass and connect them to fishing line vertically spread from heating to cooling plate. This allowed the bottom sensor movement only in a vertical direction.

2.4 Experimental arrangement

Experimental arrangement in the Barel of Ilmenau is in fig. 2.6. ODiSI-B was placed on the upper-cooling plate together with the data logger Agilent 34972A for Pt100 sensors. The optical fibre was placed either along the central axis of the cell or in the side position approximately 1.4 m from wall to measure in the area of rising plumes. In the horizontal distance 4 cm from fibre were placed two Pt100 sensors, one for measuring in the bottom BL layer and core region and second for measurements in the vicinity of the cooling plate. To exclude any strain acting on the optical fibre, it was glued to the fishing line with small deflections, which allows spreading and shrinking of polyimide coating of the fibre. Another fishing line was used for supporting lower Pt100 in the horizontal position. At the heating plate were fishing lines fixed by two small screws and optical fibre sensor was bent and fixed with adhesive tape, because last several centimetres of fibre cannot be used for measurements [24].

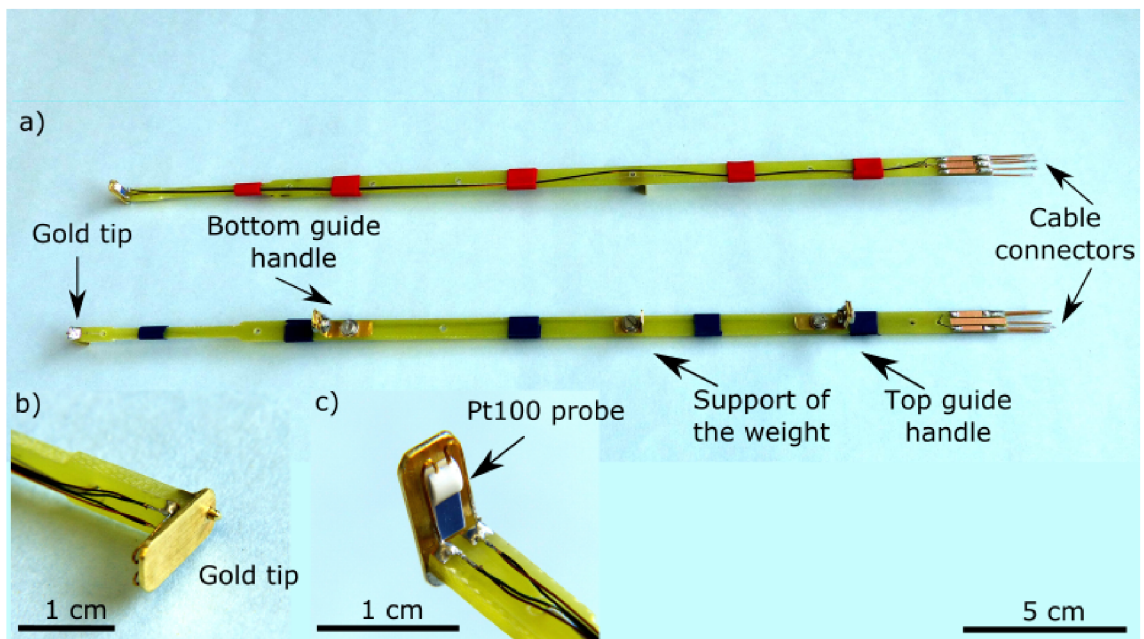


Fig. 2.5: Lower Pt100 probe for the reference temperature profiles measurements designed at ISI. a) The probe is shown from the front and back side. b) Detail view on of the gold tip which serves as the electrical indicator of mechanical contact of the probe with the bottom plate. Opposite to the tip, the small electrode made of the copper sheet is installed on the surface of the bottom plate to secure the electrical connection. c) Detail view of the Pt100 sensor fastened to the brass plate.

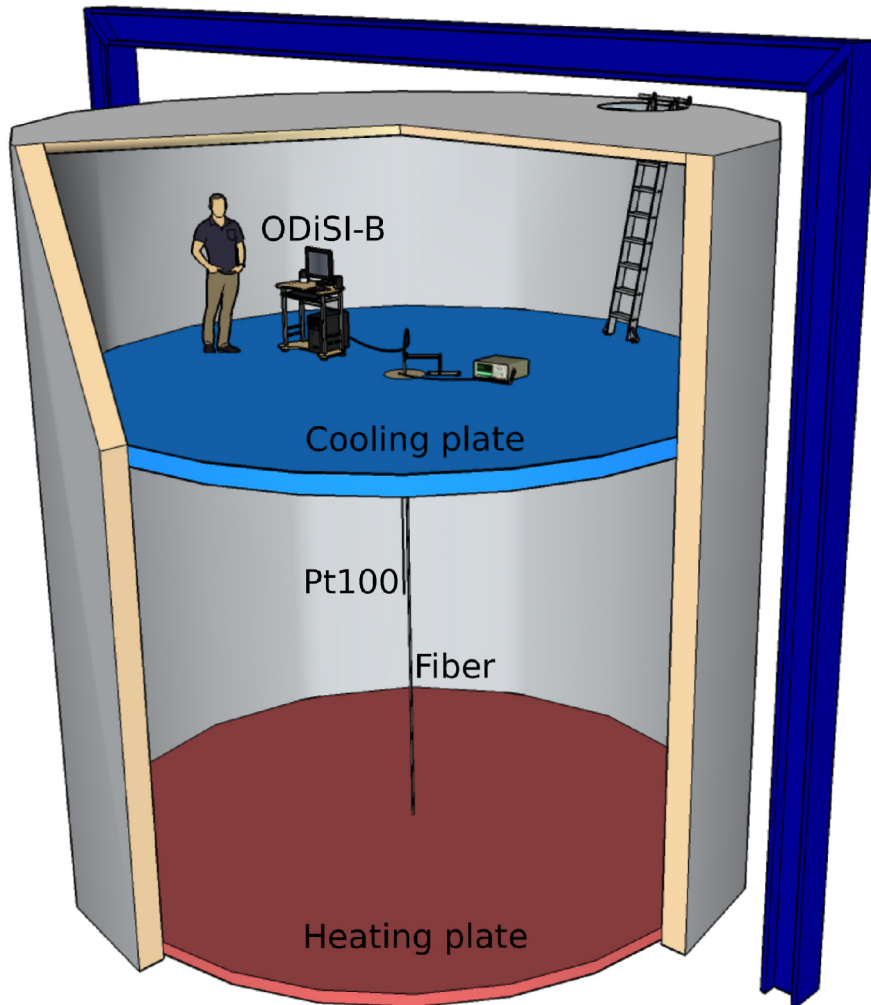


Fig. 2.6: Schematic illustration of Luna ODiSi-B and Pt100 probes installation in the axis of BOI. Luna ODiSi-B system and data acquisition unit for Pt100 probes were placed on an upper side of the top plate. The optical fibre passes through a hole in the plate and is fixed to the bottom plate. Both Pt100 probes were suspended on the feed cables passing through the hole in the top plate together with the fibre. The upper Pt100 probe serves only for measurement of temperatures profiles across the top boundary layer, whereas the lower Pt100 probe serves for measurement across the bottom layer and in the turbulent core.

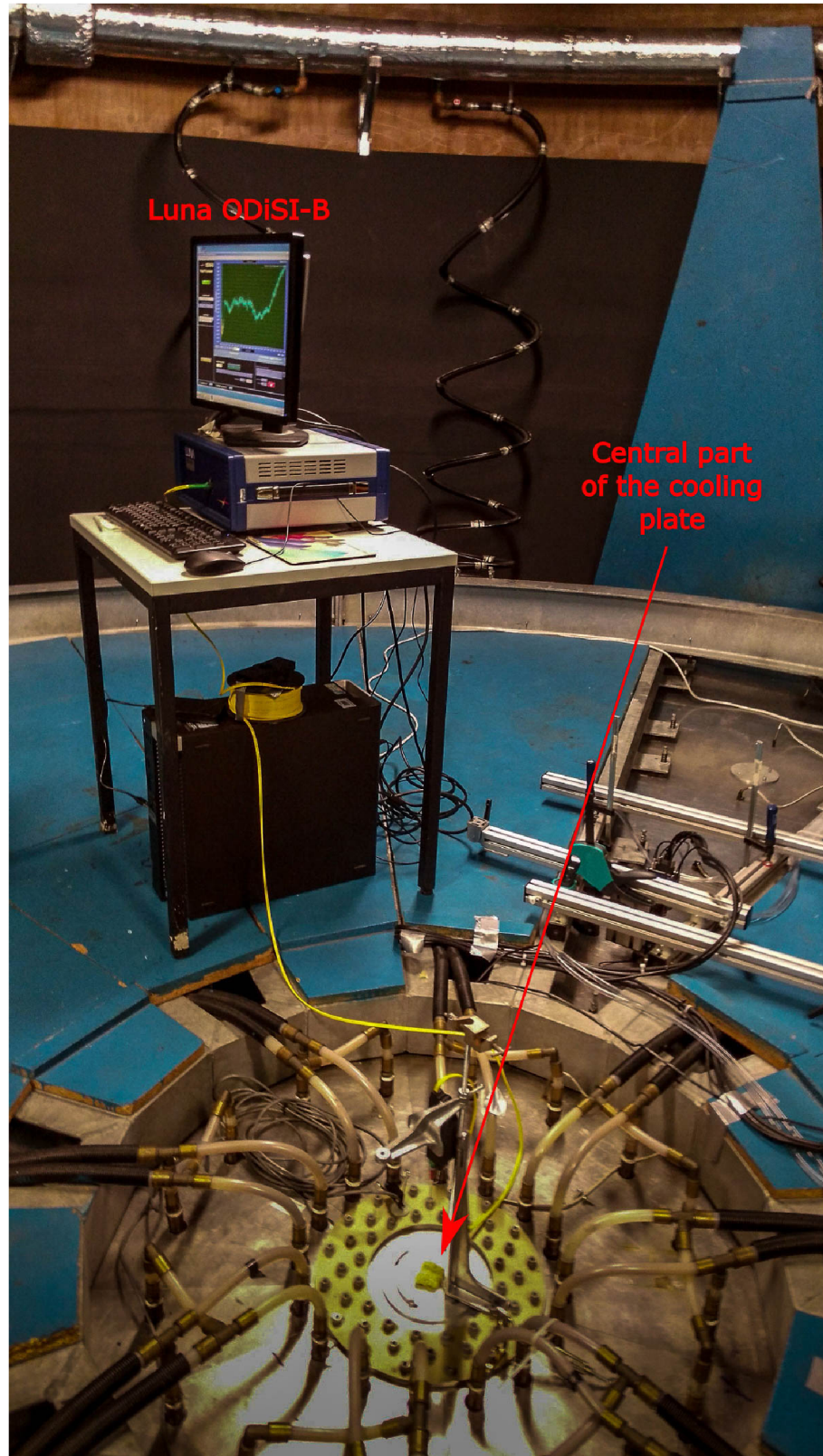


Fig. 2.7: The arrangement of Luna ODISI-B in the space above the top plate. Optical fibre sensor here enters the cell in the centre of the plate. The pipelines belong to the water cooling system of the plate.

3 RESULTS AND DISCUSSION

The time order of all measurements is described in table 3.1. Measurements were conducted within three runs:

- At the run 1, core temperature T_c in the centre of the cell was measured by one Pt100 probe. The optical fibre was placed in the central axis wrapped around the fishing line and the end of the fibre was fixed by adhesive tape (fig. 3.1). Since the last few centimetres of the fibre cannot be used for measurements, the heating plate boundary layer could not be measured. The results from the ODiSI-B were greatly influenced by the strain in the fibre and were not further evaluated.
- At the run 2, fibre attachment was improved by glueing it to the fishing line with small bends to compensate for the temperature expansion (fig. 3.2) and thus unwanted strain in ODiSI-B measurements. Reference temperatures for calibration of ODiSI-B measurements were acquired by the two Pt100 probes described in chapter 2.3, which could be moved along the fibre sensor. With this new probes, it was possible to measure temperature profiles at vertical axis with spatial resolution 5 mm.
- The experimental set-up of the run 3 was almost the same as Run 2, but the properties of fluid were measured at vertical 1.4 m from the wall in a region of raising wind flow. Before every measurement at the run 3, we visually tested the direction of the wind by a window located in the middle of the cooling plate and smoke from a small Christmas pyramid. By observations, sensors were located in the region of the rising flow of LSC. Within an observation time of 2 min, the smoke trace directed horizontally toward opposite side of sensors and oscillated azimuthally within $\sim \pm 45^\circ$ degrees around the plane created by the cell axis and sensors.

At run 1, ODiSi-B recorded temperature profiles along the fibre sensor with frequency 100 Hz for 90 min. Since the file size of the measurement was too big to be handled effortlessly, at Run 2 and 3 the frequency of recorded profiles was lowered to 10 Hz. The frequency of Pt100 measurements was always 10 Hz.

Stabilization time of the cell after the change in temperatures of the plates was at least 2 days. During this time was monitored temperature T_c and the measurements were conducted only after its stabilization.

All points in the table 3.1 were set with $T_m = 30^\circ\text{C}$ except three derogations. First is at run 1 at $\Delta T = 40^\circ\text{C}$. Since the cooling plate could not be set bellow 13°C , we changed the T_b to 53°C and T_m was thus 33°C . Second exception is at run 2 at second reference measurement with $\Delta T = 0^\circ\text{C}$ and $T_b = T_t = 20^\circ\text{C}$ which was used for calibration of ODiSI-B. Last exception is at run 2, $\Delta T = 35^\circ\text{C}$ where water

condensed at cooling plate because of high humidity in ambient air and T_c deviates bellow T_m . This was not observed for any other measurement with $\Delta T > 5^\circ\text{C}$.

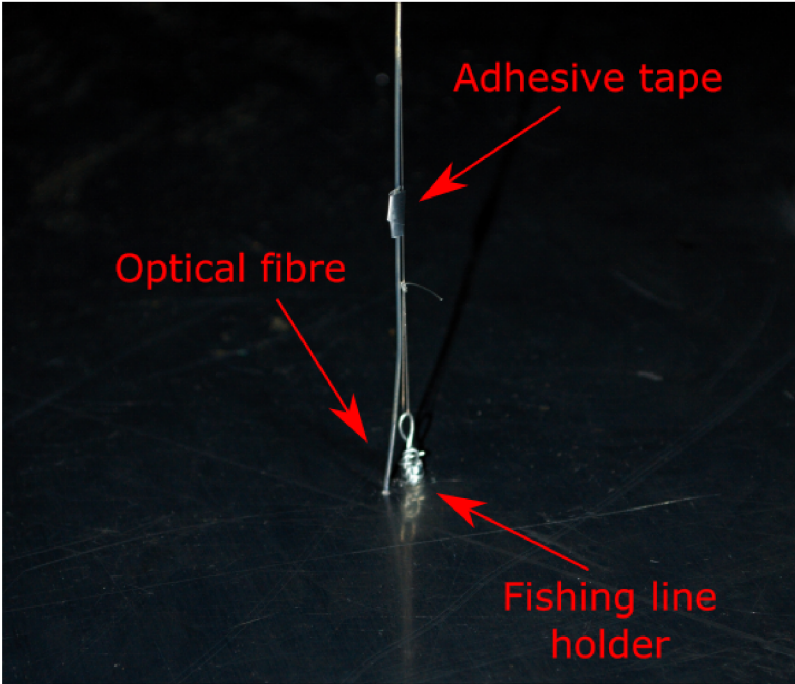


Fig. 3.1: Details of fastening the optical fibre sensor to the heating plate for run 1.

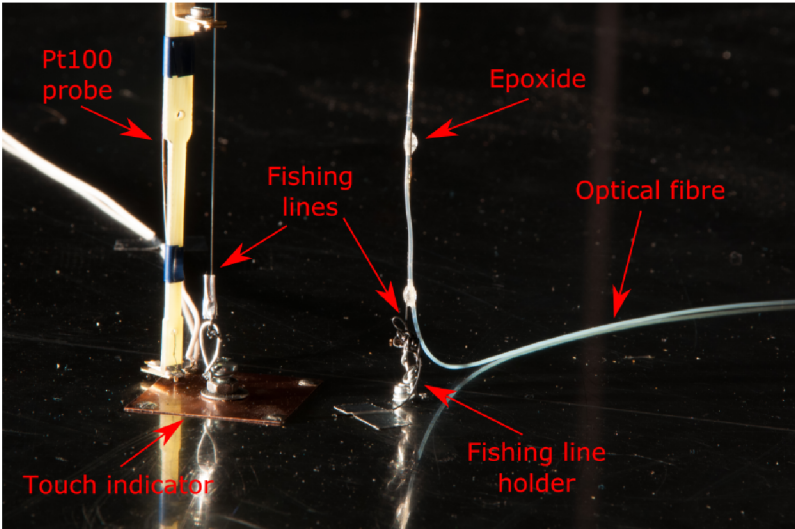


Fig. 3.2: Details of fastening the optical fibre sensor to the heating plate for run 2 and 3, where was also possible to measure the bottom BL.

Tab. 3.1: An overview of all measurements. The order of entries corresponds to the time sequence of execution. Run 1 was used only for T_c evaluation. In run 2 and 3 fixing of the optical fibre sensor was improved and two movable Pt100 probes were installed in parallel to fibre.

$\Delta T(^{\circ}\text{C})$	$T_b(^{\circ}\text{C})$	$T_t(^{\circ}\text{C})$	$T_c(^{\circ}\text{C})$	$T_m(^{\circ}\text{C})$	$T_c - T_m$	$(T_c - T_m)/\Delta T$	Ra
Run 1 - middle axis of barrel							
0	30,00	30,00	30,12	30,00	0,12		
1	30,50	29,52	30,06	30,01	0,05	0,05	1,09E+10
2	31,00	29,01	30,17	30,01	0,16	0,08	2,18E+10
5	32,49	27,49	30,19	29,99	0,20	0,04	5,45E+10
10	34,98	25,01	30,36	30,00	0,37	0,04	1,09E+11
15	37,50	22,50	30,51	30,00	0,51	0,03	1,64E+11
20	40,00	19,99	30,73	30,00	0,73	0,04	2,18E+11
25	42,51	17,51	30,87	30,01	0,86	0,03	2,73E+11
30	45,00	15,02	31,09	30,01	1,08	0,04	3,27E+11
35	47,50	12,51	31,26	30,01	1,25	0,04	3,82E+11
40	53,02	12,99	34,25	33,01	1,25	0,03	4,17E+11
0	30,02	30,03	29,88	30,03	-0,14		
2	31,00	28,99	30,04	30,00	0,05	0,02	2,18E+10
20	40,00	20,01	30,66	30,01	0,65	0,03	2,18E+11
Run 2 - middle axis of barrel							
0	30,00	30,01	29,67	30,01	-0,33		
0	20,00	20,00	19,99	20,00	-0,01		
0	30,02	30,00	29,77	30,01	-0,24		
2	31,00	29,01	29,84	30,01	-0,17	-0,08	1,81E+10
5	32,50	27,50	29,74	30,00	-0,26	-0,05	4,53E+10
20	39,99	20,00	30,46	30,00	0,46	0,02	1,81E+11
5	32,49	27,47	29,95	29,98	-0,03	-0,01	4,53E+10
35	47,49	12,50	29,23	30,00	-0,77	-0,02	3,17E+11
Run 3 - 1.4 m from side wall, vertical position							
0	30,01	30,00	29,62	30,01	-0,39		
5	32,50	27,49	30,09	30,00	0,09	0,02	4,53E+10
20	40,00	19,99	30,93	30,00	0,94	0,05	1,81E+11
30	44,99	15,00	31,14	30,00	1,14	0,04	2,72E+11

3.1 Properties of air around measurement point

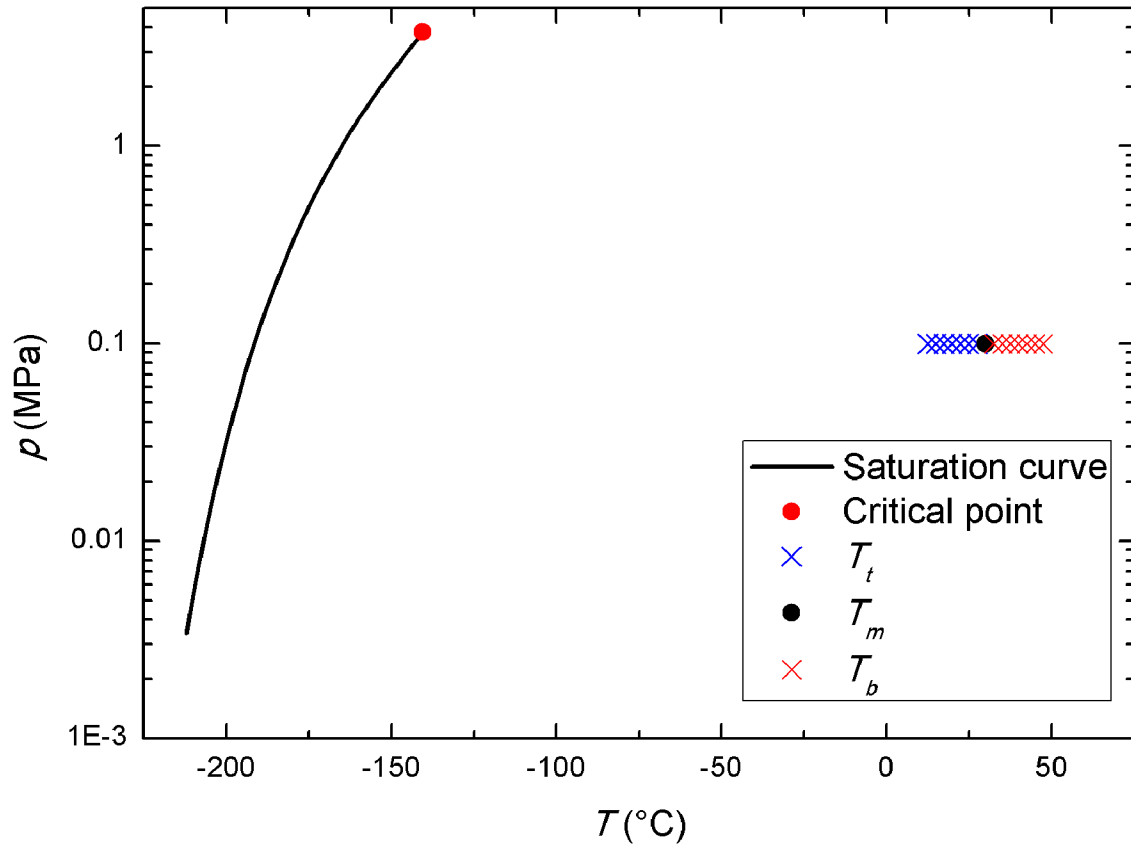


Fig. 3.3: Saturation vapour curve of the dry air and measurement point. The plate temperatures (blue crosses for different T_t , red crosses for T_b and black circle for T_m) are very distant from saturation curve (black) and critical point (red). Properties of the air should thus weakly depend on the temperature.

The saturation vapour curve of the air and measurement points are in fig. 3.3. Since the measurements were done in the temperature range from 10 to 50 °C at ambient pressure, the properties of the air varied within 10 – 20% as can be seen in fig. 3.4. Properties were nondimensionalized as $(X(T) - X(T_m))/X(T_m)$, where X is a given property and $T_m = 30$ °C. The strongest dependence on temperature can be seen in term $\alpha/\nu\kappa$ which occurs in calculation of Ra number. Comparison of the properties for different fluids (glycerol, SF₆, He) can be found in [15–17].

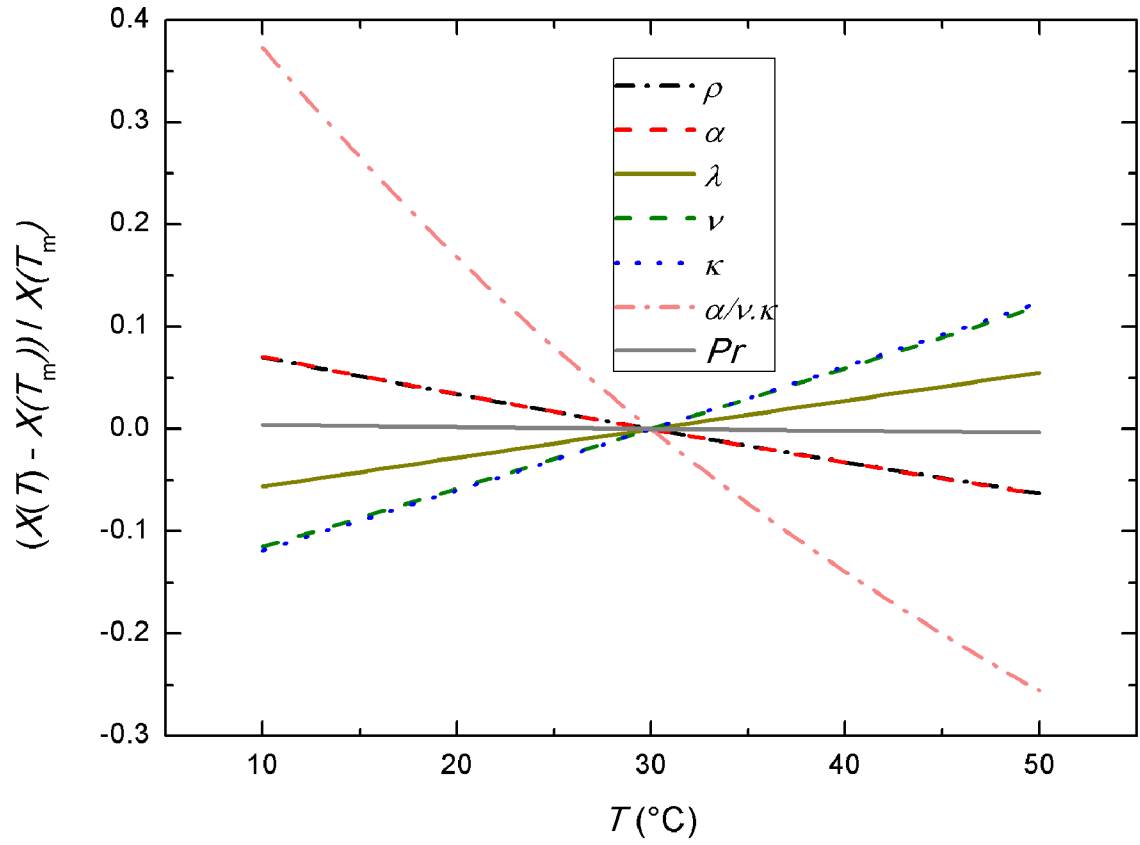


Fig. 3.4: Dimensionless properties of air. Property X was nondimensionalized as $(X(T) - X(T_m)) / X(T_m)$. $\alpha/\nu\kappa$ is the term occurring in the calculation of Ra number.

3.2 Core temperature measurements

At all measurements, core temperatures T_c were recorded by one Pt100 probe located in the vertical centre of the cell. The deviations of these temperatures at higher temperature differences ΔT from T_m can be first sign on NOB effects.

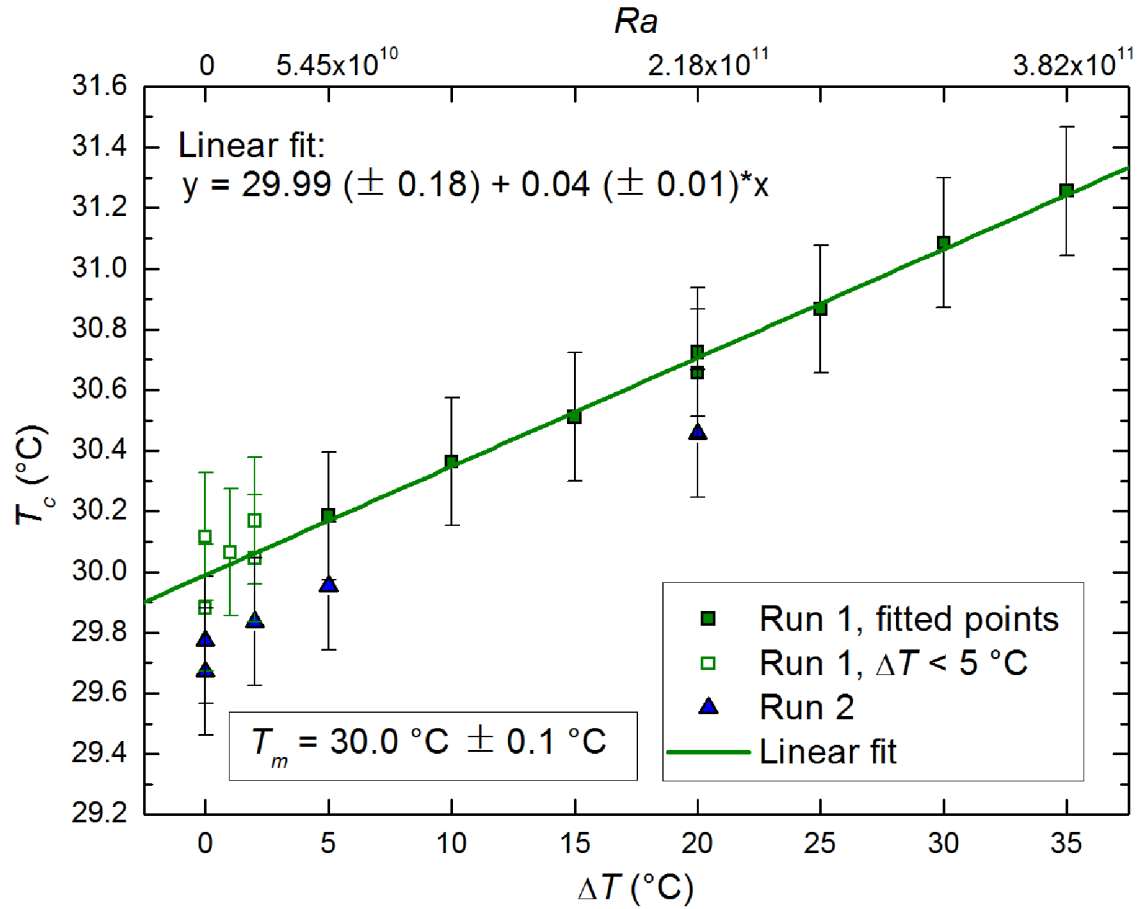


Fig. 3.5: Dependence of the core temperatures T_c measured by Pt100 probes on temperature difference ΔT between the plates (bottom axis) and Ra number (upper x axis). Points from run 1 with $\Delta T \geq 5 \text{ } ^\circ\text{C}$ are shown as green filled squares, green line is a linear fit through these points. Data from run 1 with $\Delta T < 5 \text{ } ^\circ\text{C}$ are shown as empty green squares. Blue triangles are T_c temperatures from run 2. At all measurements the T_m was set to $30 \text{ } ^\circ\text{C}$. Points are average from 90 min measurements with frequency 10 Hz.

Fig. 3.5 shows the dependence of T_c on temperature difference ΔT between the plates and Ra number (upper axis). Since the temperatures set at the plates are

much more homogeneous for $\Delta T \geq 5^\circ\text{C}$ because the pumps distributing the water along the plates could work at full power, a linear fit was conducted through the green filled squares from run 1. At our applied temperature difference, it is possible to describe dependence of T_c on ΔT as $T_c = T_m + \alpha(T_m)\Delta T$, where $\alpha(T_m)$ is constant at a given T_m . Similar linear dependence to $Ra = 2 \times 10^{13}$ was measured by [36]. This measurement suggests that strong NOB effects should be possible to observe in our data.

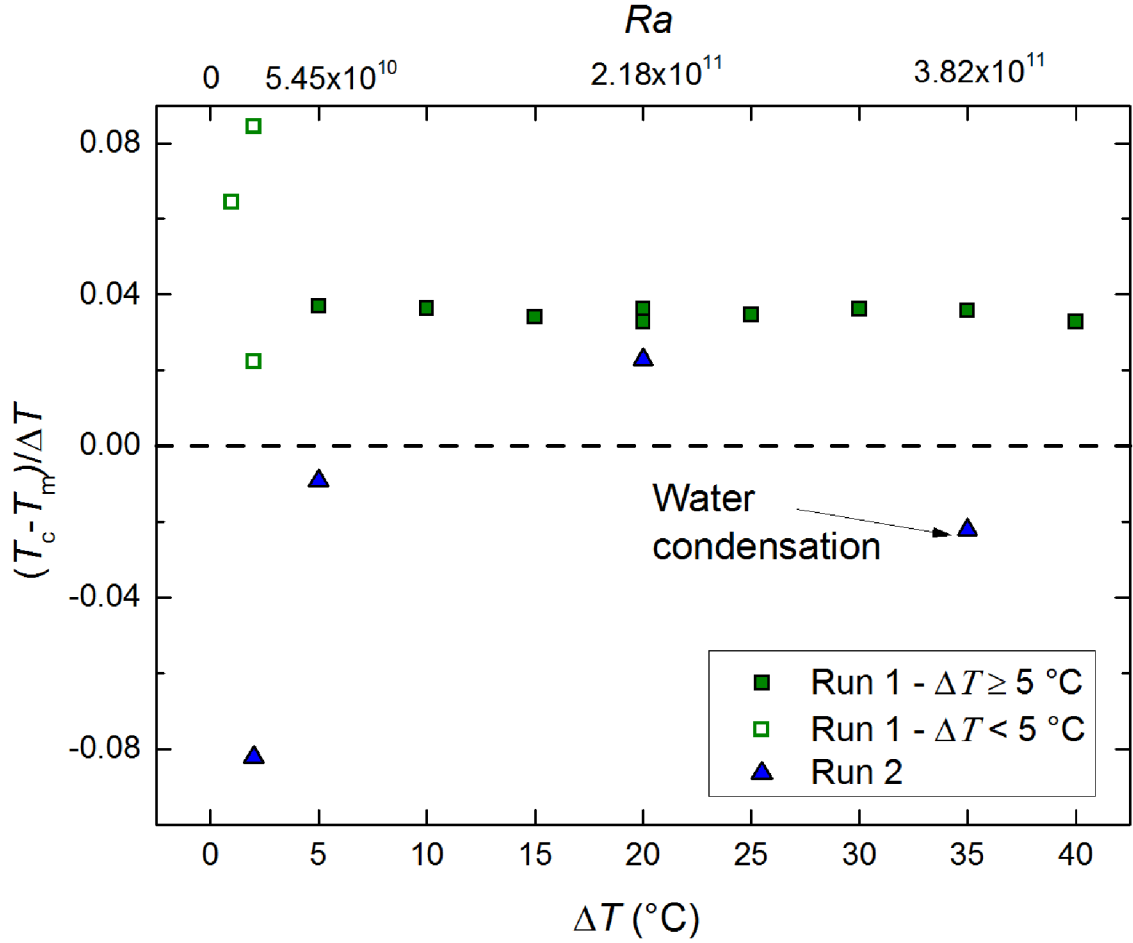


Fig. 3.6: Deviation of the core temperatures T_c from the mean temperatures T_m divided by temperature difference between the plates ΔT as a function of ΔT resp. Ra (upper x axis). Points are average from 90 min measurements with frequency 10 Hz. Symbols and colours corresponds with the fig. 3.5, green squares (run 1, filled for $\Delta T \geq 5^\circ\text{C}$ and empty for $\Delta T < 5^\circ\text{C}$) and blue triangles (run 2) were measured in the middle of the central axis. Deviation are relatively uniform from $\Delta T > 5^\circ\text{C}$. Irregularity below and at 5°C are probably caused by inaccurate temperature distribution at the plates.

Deviations of the core temperature T_c from mean temperature T_m divided by temperature difference ΔT between the plates as a function of ΔT resp. Ra (upper horizontal axis) are in fig. 3.6. Large scatter of deviations at smaller ΔT is probably due to insufficient temperature distribution across the plates. Big deviation at the point from run 2, $\Delta T = 35^\circ\text{C}$ was caused by water condensation at the cooling plate. Water condensation altered the heat transfer at the cooling plate and thus changed temperature profile. Uniformity of deviations within span of $\Delta T = 5 - 40^\circ\text{C}$ corresponds to linear dependence in fig. 3.5.

3.3 Temperature profiles

This chapter presents a measurement of the temperature profiles at two different verticals in the cell. Firstly, temperature profiles measured by Pt100 probes will be evaluated. These profiles will be then used for calibration of ODiSI-B. Calibration process will be described in the chapter 3.3.3. The last section presents the comparison between the temperature profiles measured with both methods.

3.3.1 Temperature profiles by Pt100 probes

Comparison of time-averaged temperature profiles by Pt100 probes $\langle T_{Pt}(z) \rangle$ for two measurements at $\Delta T = 20^\circ\text{C}$ is in fig. 3.7. Two profiles were measured. One along the middle axis (Run 2, central position) and the other along a vertical 1.4 m from the side wall (Run 3, side position). The temperature of the side profile is higher along the full length of the cell which is reasonable as the side position corresponds to the position of raising hot flow. The uncertainties of the temperature profiles are in fig. 3.8. The standard deviation $\sigma_{Pt}(z)$ for every point was computed from 1 min measurements with frequency 10 Hz as

$$\sigma_{Pt}(z) = \sqrt{\frac{1}{N-1} \sum_{i=1}^N |T_{Pt}(z) - \langle T_{Pt}(z) \rangle|^2}, \quad (3.1)$$

where N is the number of measured values. In BL layers region, the uncertainty drastically increased.

To be able to compare our data with other cells, we used two non-dimensional parameters from the work of Ahlers et al. [37]. First one is a non-dimensional temperature

$$\Theta(z, r) \equiv \frac{\langle T(z, r, t) \rangle_t - T_m}{\Delta T}, \quad (3.2)$$

where r is the radial position from central axis. The second one is the non-dimensional parameter for radial position

$$\xi \equiv \frac{R-r}{R}, \quad (3.3)$$

where R is the diameter of the cell.

Temperature profiles data from run 2 and 3 acquired by Pt100 probes are plotted in fig. 3.9. Temperatures $\Theta(z, r)$ are shown as a function of a non-dimensional distance from the heating plate z/L , where L is the height of the cell. The temperature profiles at the central axis are marked as triangles and for the side position

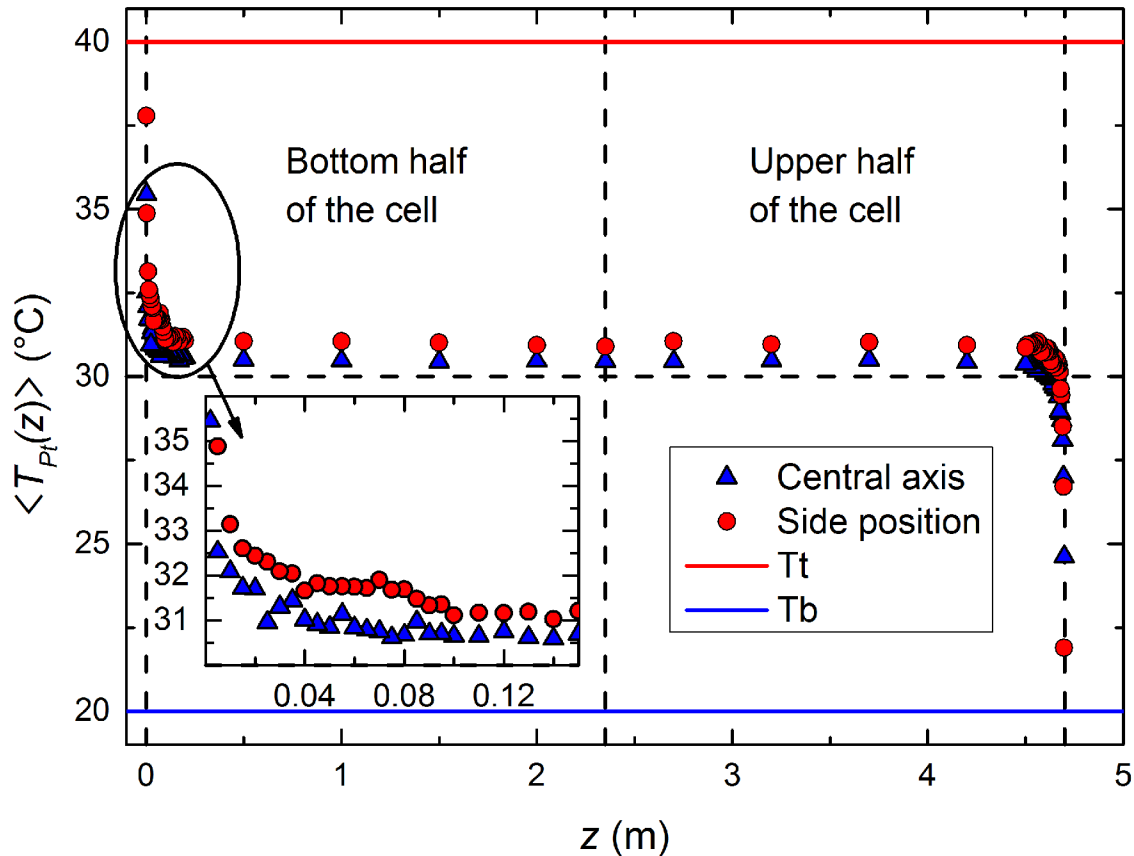


Fig. 3.7: Time-averaged temperature profiles $\langle T_{Pt}(z) \rangle$ as a function of distance z from the bottom of the heating plate measured by Pt100 probes ($\Delta T = 20^\circ\text{C}$; $Ra = 2.18 \times 10^{11}$). The vertical dashed black lines indicate the location of the cell centre and the plates position. The blue filled triangles represent the measurements along the central axis of the cell, the red filled circles represent the measurements along the axis 1.4 m away from the cell sidewall. The inset shows detailed view on the profiles in the region of the bottom boundary layer. The solid horizontal lines represent the mean temperatures of the top (T_t - blue line) and bottom (T_b - red line) plates. The points are average from 1 min measurements with frequency 10 Hz. [12]

as circles. Two profiles at the central axis deviate from prevailing trend of temperature $\Theta > 0$ in the core region as can be seen in this inset. For $Ra = 5.45 \times 10^{10}$ ($\Delta T = 5^\circ\text{C}$) this is probably caused by low temperature difference and insufficient flow stabilization in the Barrel. For $Ra = 3.82 \times 10^{11}$ ($\Delta T = 35^\circ\text{C}$) the difference is caused by water condensation at the cooling plate.

To find out the influence of the wall on the temperature profiles measured in the side position, we compared our data with data from Ahlers et al. in fig. 3.10. In this work authors used sulfur hexafluoride (SF_6) with very similar $Pr = 0.8$, but different aspect ratio $\Gamma = 0.5$. Ra number in their work covered range from $10^{12} - 10^{14}$ and

sensors were nearer to the side wall ($\xi = 0.268$). By comparison of our data with $\xi = 0.3846$ (circles) and data from Goettingen with $\xi = 0.2680$ (black and orange squares) we can see that the slope of points in the core region is much bigger for data from Goettingen and thus our side measurement is not highly affected by sidewalls.

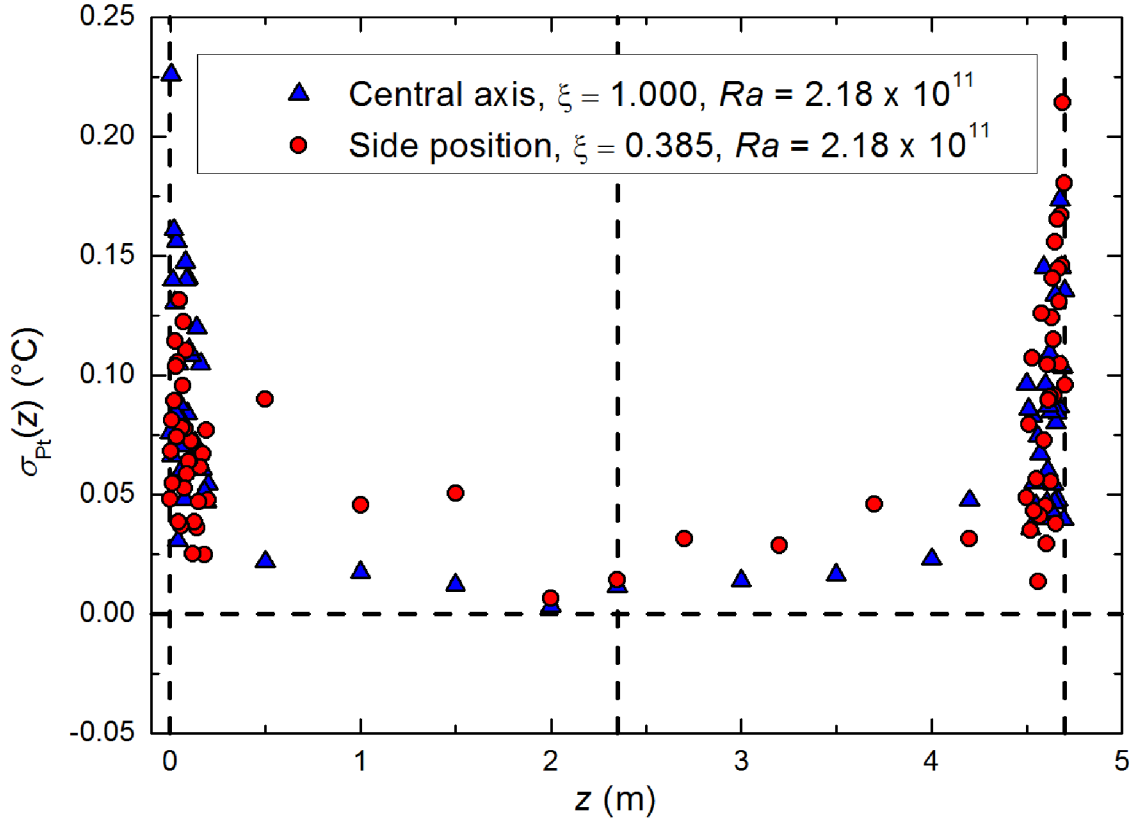


Fig. 3.8: Standard deviation $\sigma_{Pt}(z)$ of temperatures from fig. 3.7 measured by Pt100 probes at $\Delta T = 20^\circ\text{C}$ ($Ra = 2.18 \times 10^{11}$) at central axis (blue triangles) and 1.4 m from the wall (red circles). The standard deviation are computed from 1 min measurements with frequency 10 Hz.

The BL region was in detail measured by du Puits et al. [21]. In the fig. 3.11 we show the comparison of the temperature profiles at both plates as the function of z/L . In this case, Θ was computed as

$$\Theta_b(z) = 2[T_b - T(z)]/[T_b - T_t] \quad (3.4)$$

for heating plate and

$$\Theta_t(z) = 2[T(z) - T_t]/[T_b - T_t] \quad (3.5)$$

for cooling plate. The data of du Puits et al. were measured by glass encapsulated microthermistors of size $125\ \mu\text{m}$, in the vertical direction. For reference, vertical

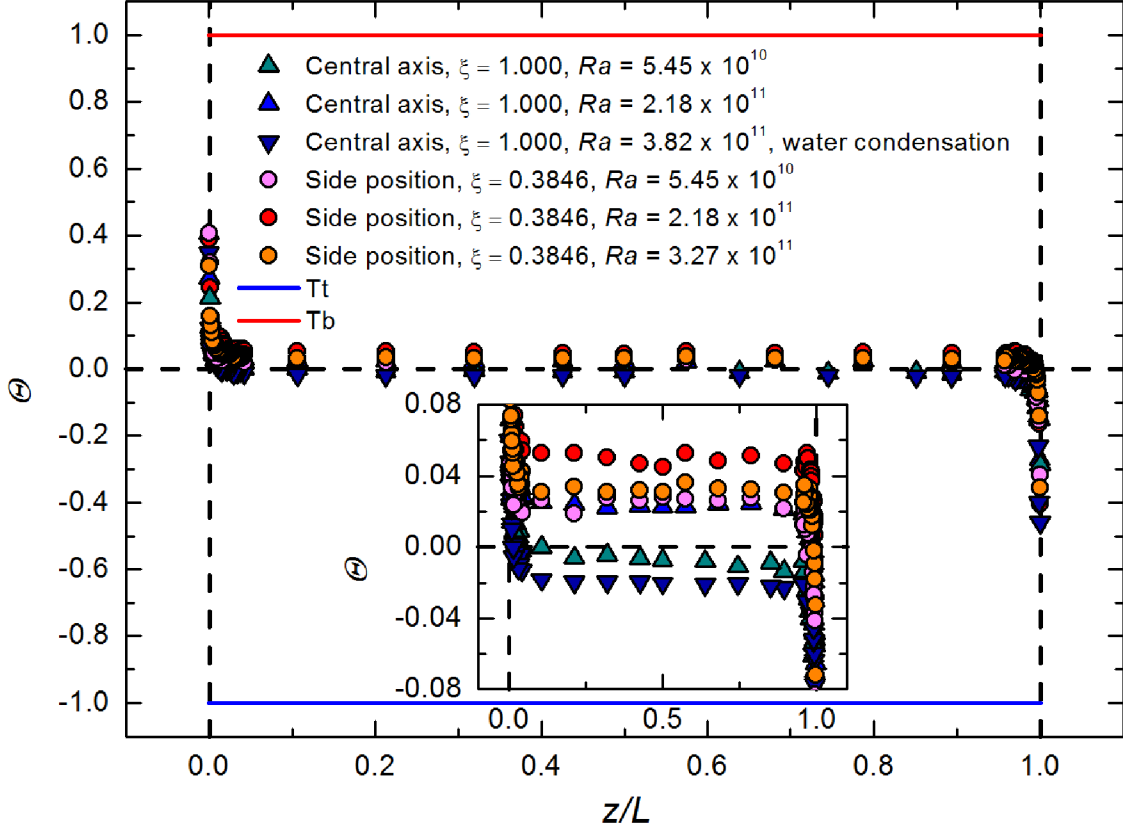


Fig. 3.9: Temperatures profiles measured by Pt100 probes plotted as dependence of non-dimensional temperature Θ on height of cell z/L . Profiles from run 2 - central axis are depicted as triangles, profiles from run 3 - side position are shown as circles. Cooling (heating) plate is marked as blue (red) line. Inset shows the core region in more detail.

dimension of our Pt100 probe was ~ 1 mm. The temperatures measured by micro-thermistors are average from 90 min with frequency 200 Hz, the vertical region of the measurements was from 70 μm to 150 mm.

One of the definitions of BL thickness uses the intersection of the mean temperature gradient at the wall with the asymptotic bulk temperature [10, 38]. In our case, the first one is led by points in BL layer and temperature of the desk, second goes through points in the core region. The intersection of these two curves then defines the thickness of the BL. This definition is used in fig. 3.12, where two temperature profiles are plotted for $\Delta T = 20^\circ\text{C}$ at the heating plate, blue triangles corresponds to the position at the central axis and red circles to the side position. Both linear fits are shown as blue or red dashed lines for central axis or side position, respectively. In the inset, the resulting BL thickness is delimited with green and gray dash-dot lines for central ($\lambda_b = 5.87$ mm) and side position ($\lambda_b = 8.67$ mm).

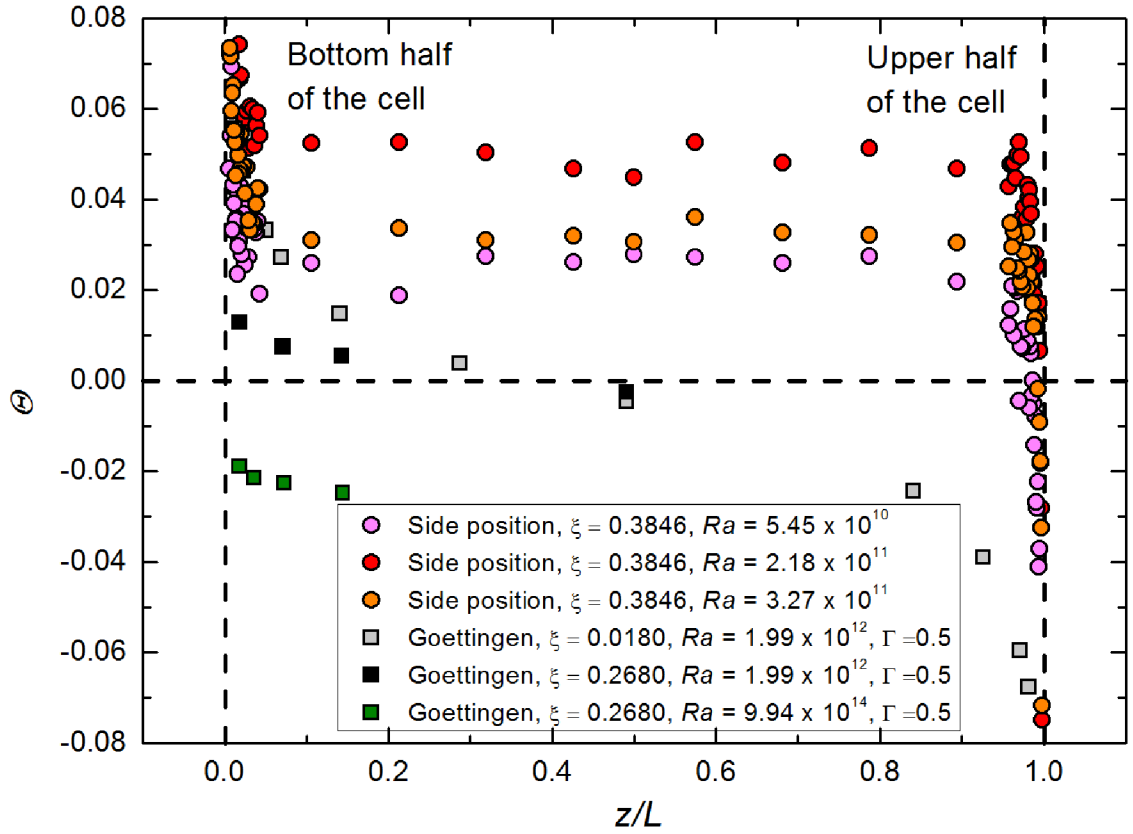


Fig. 3.10: Comparison of measurements by Pt100 probes and measurements for different radial position from [37]. Circles mark side position measurements from run 3, squares are digitalized experimental points of Ahlers et al from the cell located in Goettingen. These profiles are substantially tilted at the core region.

Dependence of the BL thickness λ_b , λ_t on the temperature difference ΔT is in the fig. 3.13. Triangles correspond to central axis measurements and circles to side position. Blue points are the BL thickness λ_b at the cooling plate, red points show the BL thickness λ_t at the heating plate. The overall trend of increased thickness at the cooling plate region and decreased thickness at the heating plate region corresponds to the measured dependence of T_c at ΔT in the fig. 3.5. The higher core temperature T_c corresponds to higher temperature difference and thickness in the cooling plate BL and visa versa for heating plate BL. In the case of water condensation, there is a drastic increase of the BL thickness.

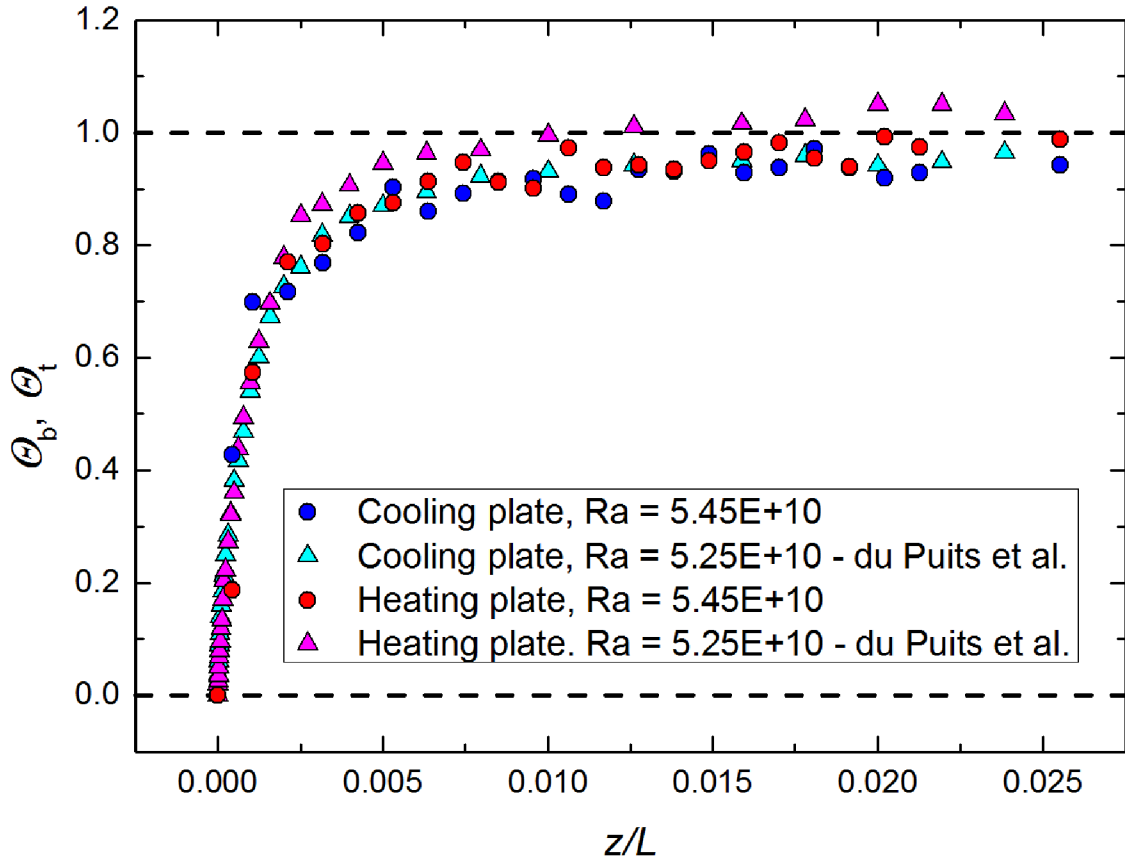


Fig. 3.11: Comparison of the BL temperature profiles with [21]. Aspect ration Γ was set ~ 1.5 at both experiments. Blue and red triangles were measured by du Puits et al., blue and red circles are our measurements for the central axis with $\Delta T = 5^\circ\text{C}$. Both temperature profiles at heating plates θ_b and cooling plates θ_t correspond to each other very well. It can be seen that du Puits et al. measured the BL region with much higher spatial resolution.

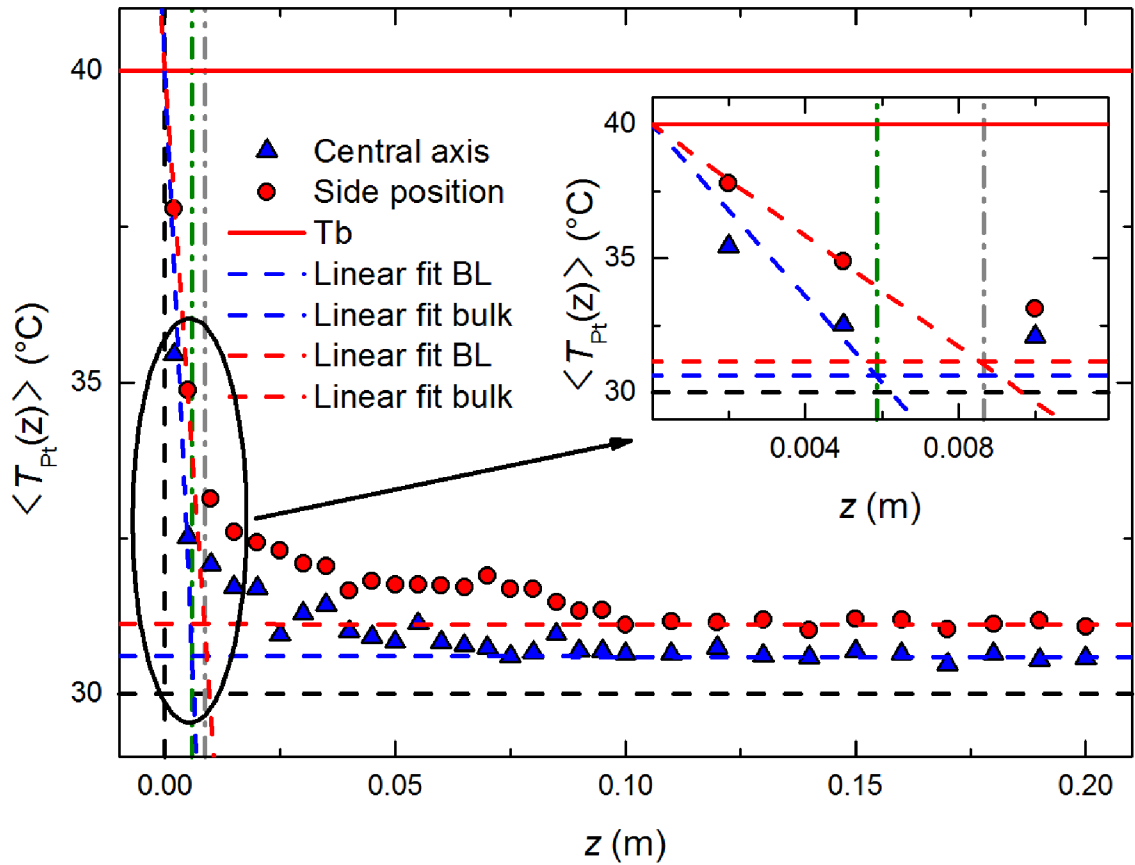


Fig. 3.12: Enlarged fig. 3.7. Thicknesses of the BL layers λ_b , λ_t are determined as intersection of the linear fits to $T(z)$ dependence near the plate and in the core region. Resulting BLs for $\Delta T = 20^\circ\text{C}$ are delimited with green and gray dash dot lines.

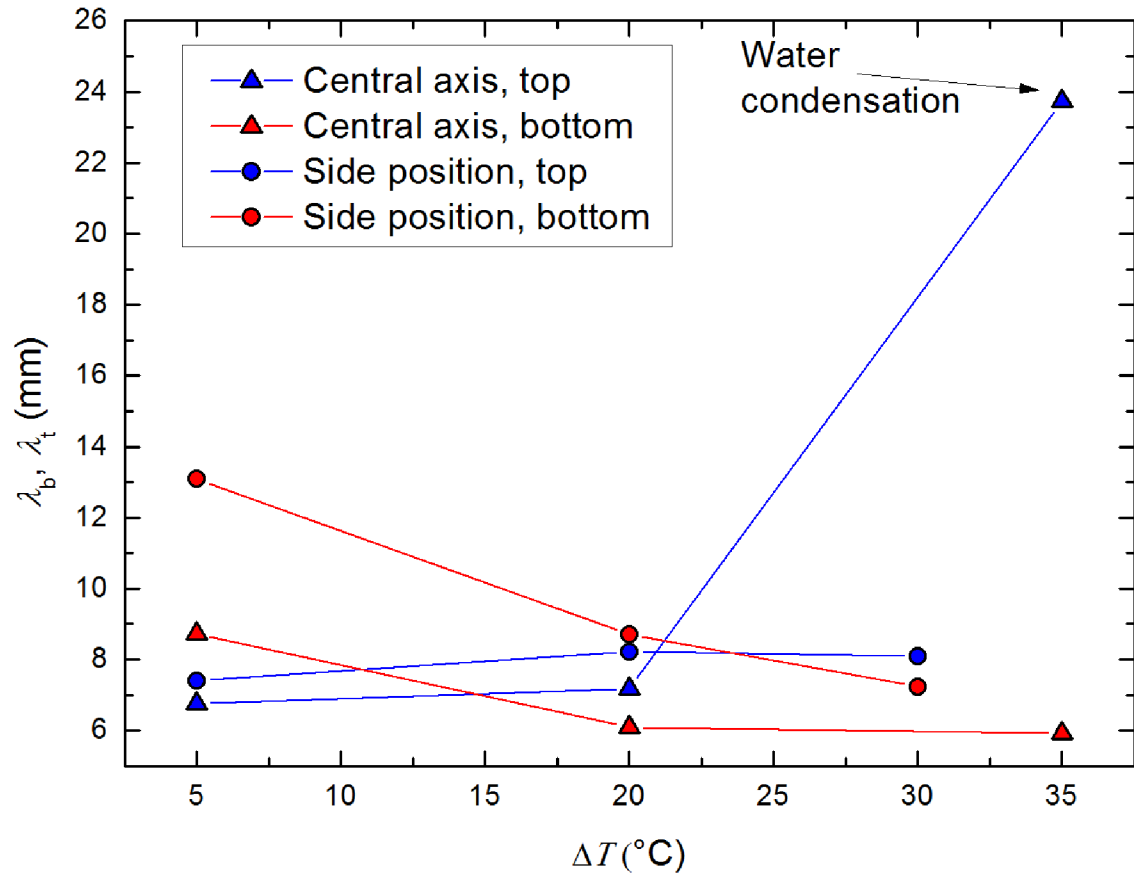


Fig. 3.13: BL thickness at heating (λ_b) and cooling (λ_t) plate for all measurements from run 2 (triangles) and 3 (circles) with $\Delta T \neq 0$ from table 3.1. The BL layer was greatly enhanced in the case of water condensation at cooling plate.

3.3.2 Frequency shift and taring

In this chapter will be mostly presented results of ODiSI-B measurements. First of all, it was necessary to find out what is the best possible processing of these measurements. Software supplied with the device allows direct conversion of frequency shift, which is basic quantity measured by ODiSI-B, to relative temperature. Nevertheless, during the run 1 we find out that this conversion at least in current experimental setup does not correspond with Pt100 probes measurements. The difference in some cases was higher than 10°C. After the email correspondence with a representative of the ODiSI-B producer in Germany, we decided to perform own calibration of the device for the correct conversion of frequency shift to temperature. The manufacturer was familiar with the fact, that conversion is not strictly linear in most cases (as supposes implementation in the device) and sent us a document [39], which describes how this calibration should be done. This document was uploaded to Turbase database [11], where the rest of data is possible to download. The linear conversion from frequency shift Δf (GHz) to temperature difference ΔT (°C) delivered by producer is approximately

$$\Delta T \sim -0.801 \left(\frac{^{\circ}\text{C}}{\text{GHz}} \right) \Delta f. \quad (3.6)$$

”Raw” frequency shift Δf - without any postprocessing from the user side is plotted in the fig. 3.14a for the central axis and in the fig. 3.14b for the side position as function of the time t and the length z_f along the fibre sensor. To distinguish clearly the flow structures we plotted only 1000s time window from 5400s measurements. The value of frequency shift is expressed by colours. The red colours describe the lowest frequency shifts and the highest temperatures (eq. 3.6). Blue colours describe the highest frequency shifts and the lowest temperatures. Heating plate is located at $z = 0$ m and cooling plate at $z = 5$ m, ~ 30 cm of the fibre was ”lost” in bends between fixating points and a heating plate (see fig. 3.2). Direction z_f in the ODiSI-B measurement therefore accurately describes location at the fibre sensor, not the distance from the heating plate. Artefacts of the optical fibre sensor can be seen at both figures as horizontal lines along the entire time axis. These lines probably correspond to some degraded parts of the optical fibre sensor that gives constantly altered the signal.

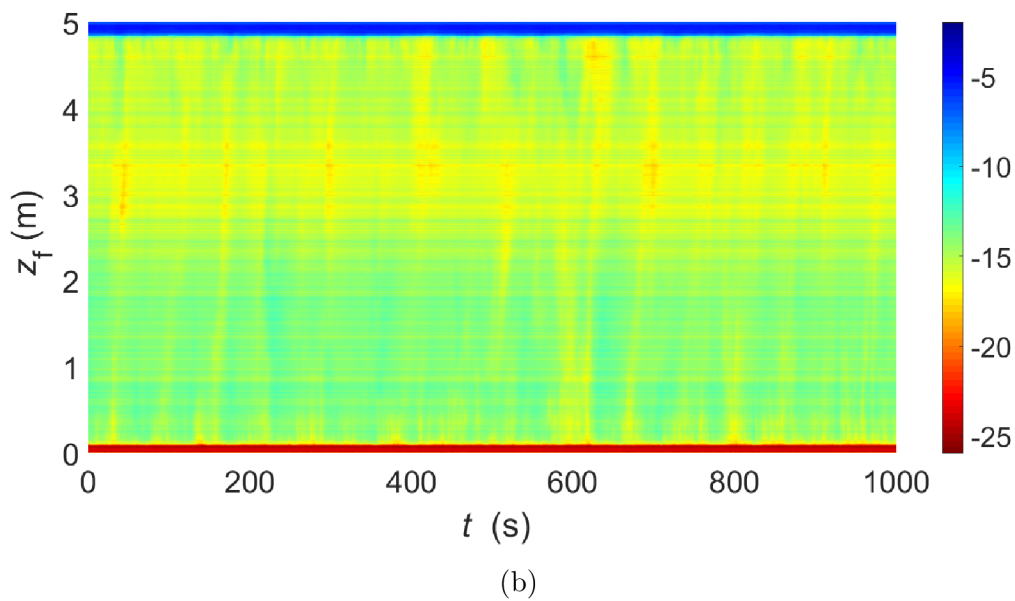
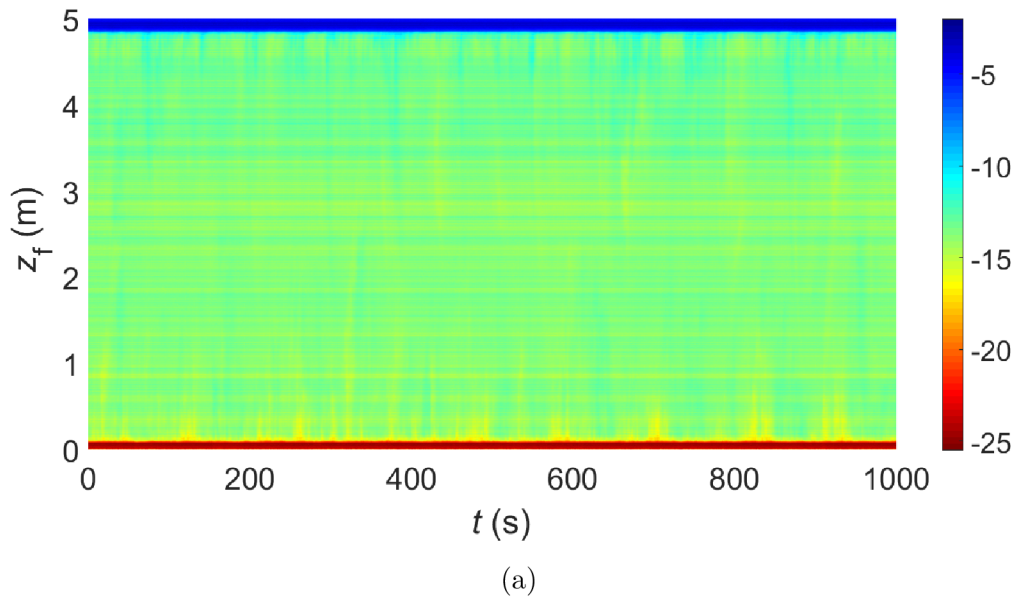


Fig. 3.14: Dependence of the frequency shift Δf on the time t and position z on the fibre sensor for $\Delta T = 20^\circ\text{C}$ a) run 2 - central axis b) run 3 - side position. The frequency shift is expressed by colour map, low frequency shift (high temperatures) are shown by red colours and vice versa, high frequency shifts (low temperatures) are shown by blue colours. By comparison of these two plots it is visible that the overall core temperature was higher at side position.

To exclude any other phenomena (strain, microbending) than temperature from the ODiSI-B measurements, it is important to subtract a reference measurement called tare. By this technique it is possible to remove artefacts of the fibre sensor and acquire the relative values of temperature profile to some known point, which in our case should be core measurement by Pt100. In the case of known calibration, this procedure would secure the absolute temperatures along the fibre sensor.

Taring process for the central axis is shown in fig. 3.15. All windows show the dependence of frequency shift at the position on the fibre sensor z from the bottom plate. In the upper windows, the reference measurement (tare) is shown, which was measured at equal temperatures at both plates $T_b = T_t = 30^\circ\text{C}$. In the middle window, mean frequency shift measured at $\Delta T = 20^\circ\text{C}$ is plotted. Both curves were measured 90 min by frequency 10 Hz. The lower plot shows tared frequency shift which was created by subtracting the reference measurement from mean frequency shift.

In the core region, this curve should be relatively linear as can be seen from Pt100 probe measurements, which do not correspond with the increased frequency shift region from $z_f > 3\text{ m}$. We acknowledge that fluctuations along the fibre sensor are much smaller in a tared curve, but the overall trend is better in the raw measurement in the middle window. Note that for smaller ΔT measurements, the overall trend after tare was much more curved. The same figure for side position is in the fig. 3.16. Tared frequency shift again deviates from constant core region at $z_f > 3\text{ m}$. For both central and side position, the Δf in the core region is lower than zero, which correctly corresponds with $T_c > T_m$.

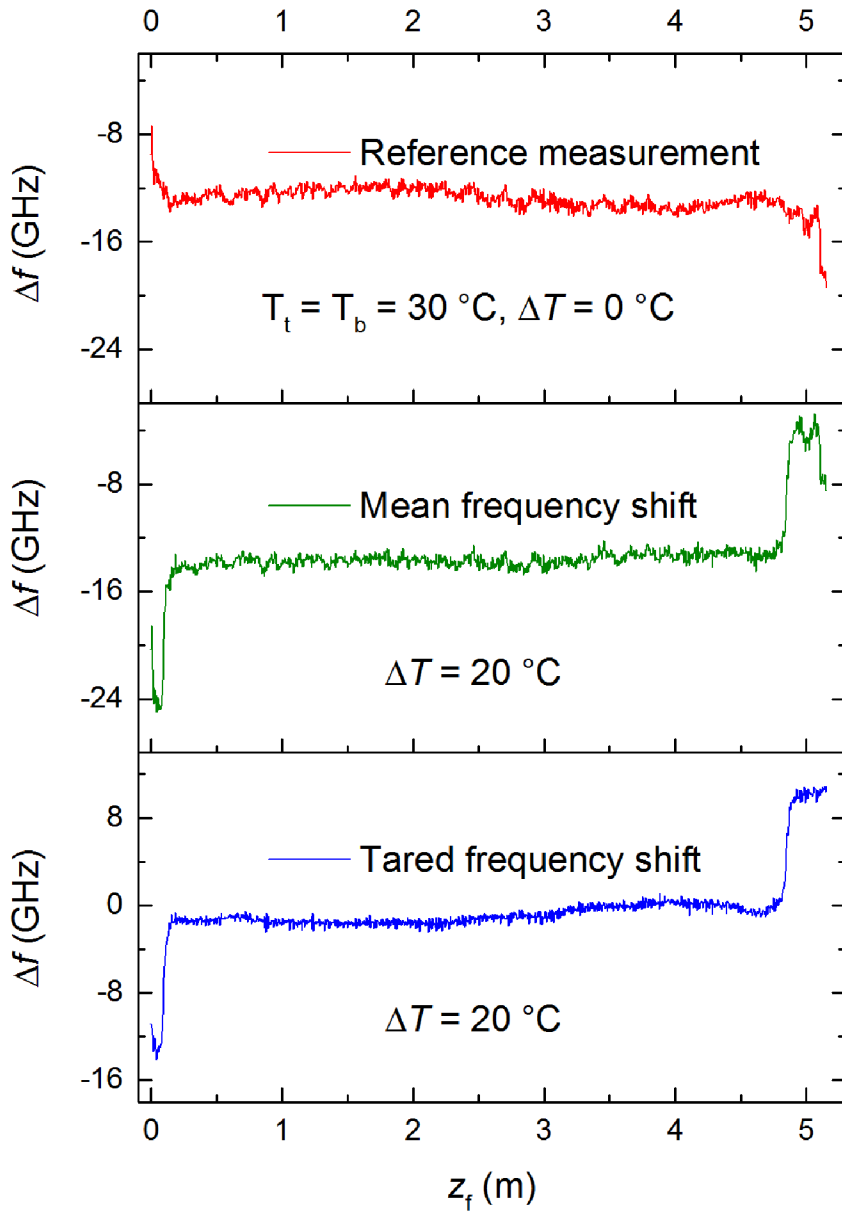


Fig. 3.15: Representation of the taring process for central axis, $\Delta T = 20^\circ\text{C}$. All graphs show dependence of frequency shift on the height z_f along the fibre sensor. Upper window shows reference measurement, so called "tare", measured at steady conditions in the cell with $T_m = T_t = T_b = 30^\circ\text{C}$. In the middle window, mean frequency shift at $\Delta T = 20^\circ\text{C}$ is plotted. By subtracting the upper tare measurement from middle one with applied temperature difference, we acquire tared frequency shift in bottom window. This curve should represent frequency shift without any artefacts from strain or perturbed structure in the fiber. However, the core region is not constant as the ones shown in temperature profiles obtained by Pt100 probes (fig. 3.7).

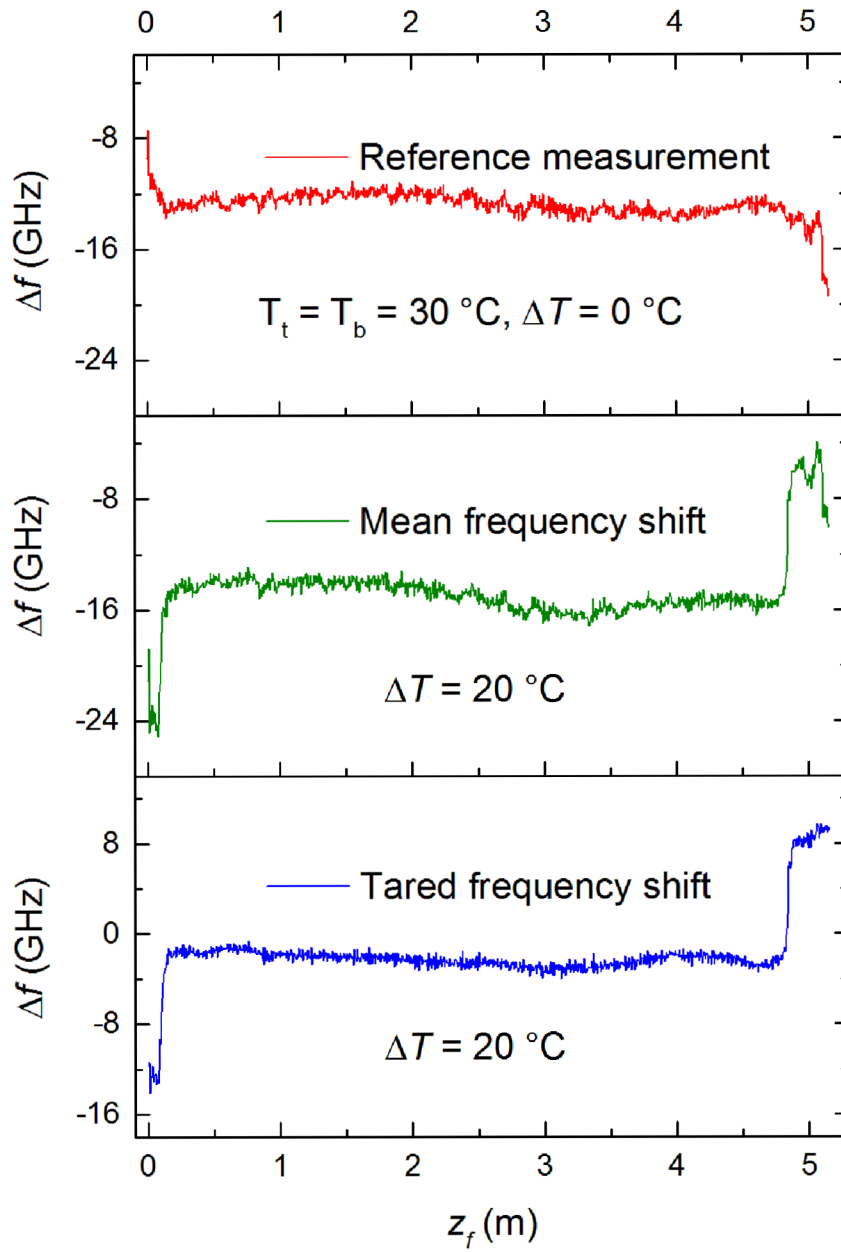


Fig. 3.16: Representation of the taring process for side position, $\Delta T = 20\text{ }^\circ\text{C}$, arrangement and description are the same as in the fig. 3.15.

3.3.3 Calibration

Measurement at the side position with $\Delta T = 30\text{ }^\circ\text{C}$ was chosen for representation of the calibration because with large temperature difference the other influences from the strain, humidity or fibre sensor perturbations significantly lesser contribute to the measured frequency shift. Visualization of one of very simple possible calibrations is in fig. 3.17. Again the mean frequency shift as the function of position z from the heating plate is plotted. Three blue points illustrate the points which were used for calibration. Two of them are located at the plates and were measured by sensors located inside the plates, which are part of the BOI apparatus. The third point is used from core measurements, which are depicted for example in the fig. 3.5. Since the temperatures are known in these three points, they create the three points calibration covering full temperature span in the Barrel. In this calibration, we suppose that the optical fibre sensor has the temperature of its environment (plates, core). The calibration curve is shown in the inset as the dependence of temperature of calibration points $\langle T_{Cal}(z) \rangle$ at mean frequency shift $\langle \Delta f \rangle_t$. Even with this easy calibration process, the calibration curve is not linear, as the manufacture propose.

Author is well aware of the more sophisticated calibration processes, that would use all temperature points measured by Pt100 probes, but since the BL thickness is only order of cm, it is very difficult to assign exactly the position z_f on the optical fibre sensor to the height z of the Pt100 probe above the heating plate (see the installation of the fibre sensor in the BOI in run 2 and 3, fig. 3.2).

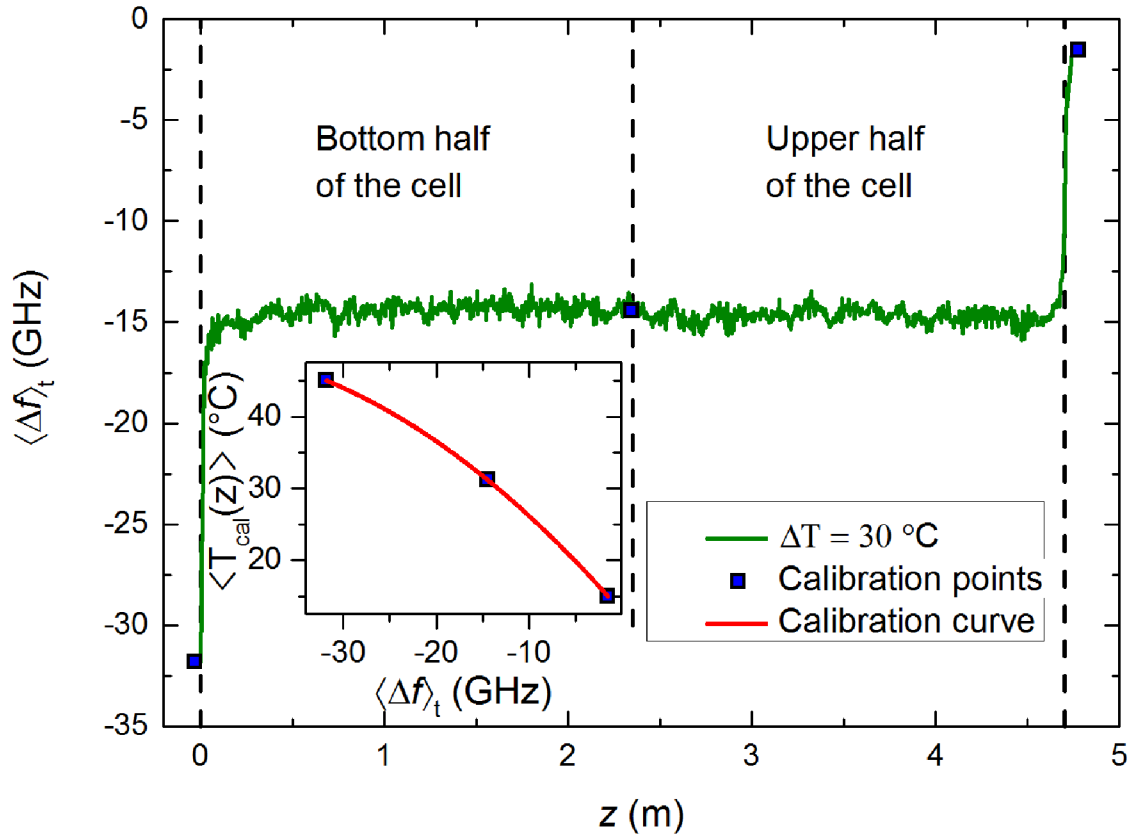


Fig. 3.17: The time-averaged frequency shift as a function of the vertical distance z from the bottom plate ($\Delta T = 30^\circ\text{C}$, $Ra = 3.27 \times 10^{11}$) measured in a vertical 1.4m from the cell side wall. In this plot the position on the optical fibre sensor was converted to the height above the heating plate. The vertical dashed black lines indicate the location of the cell centre and the positions of the plates. The inset represents a calibration curve used for transformation of the time-averaged frequency shift to the time-averaged temperature $\langle T(z) \rangle$. The red curve is second order polynomial fit of the three selected data points shown as blue squares. The temperature $\langle T_{cal}(z) \rangle$ of the middle point was measured by the lower Pt100 probe, the other two points were measured by sensors placed in plates.

3.3.4 Temperature profiles by ODiSI-B

Temperature profile created by applying the calibration curve in the fig. 3.17 to a frequency shift in the same measurement is depicted in the fig. 3.18 and compared with Pt100 probe measurement. As can be seen in the inset, the temperatures in the BL region, which was the main region of our interest, do not match very well. From this reason, we decided to use ODiSI-B measurements mainly for evaluation of correlation functions of fluctuations described in the next chapter, which can be evaluated directly using negative values of the frequency shift.

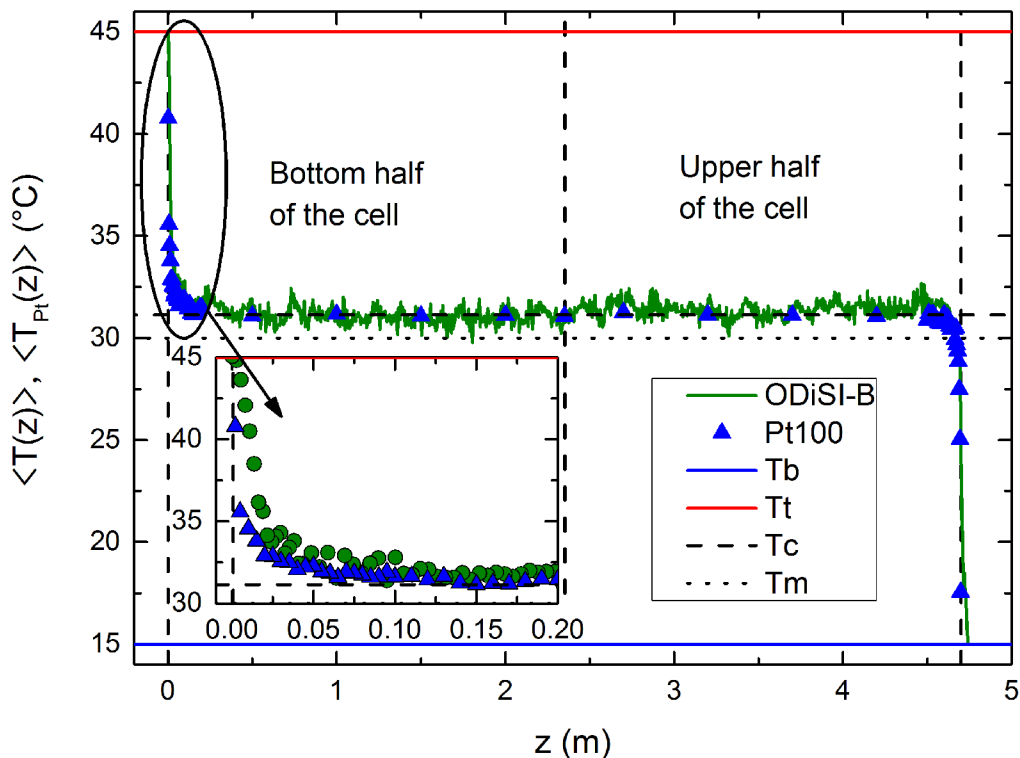


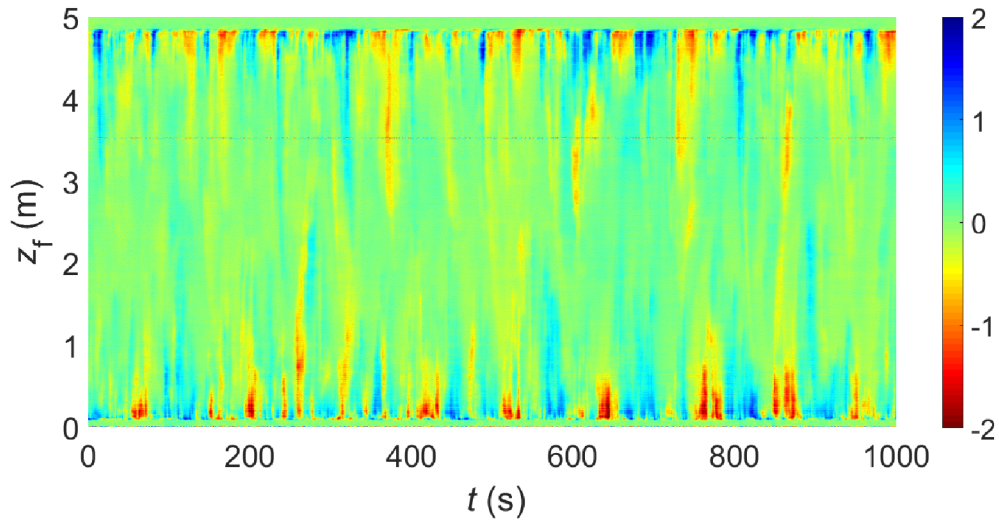
Fig. 3.18: Comparison of the time-averaged temperatures measured by Luna ODiSI-B (green solid curve, filled green circles) and Pt100 probes (blue filled triangles) as a function of distance z from the bottom plate ($\Delta T = 30^\circ\text{C}$, $Ra = 3.27 \times 10^{11}$). Both profiles were measured at side position. The vertical dashed black lines indicate the location of the cell centre and the plates. The solid horizontal lines represent the time-averaged temperatures of the top (T_t - blue line) and bottom (T_b - red line) plates. The horizontal dotted black line corresponds to the time-averaged mean plate temperature T_m . The dashed black line represents the time-averaged turbulent core temperature T_c measured in the cell centre by Pt100 probe. [12]

3.4 Fluctuations and coherent structures

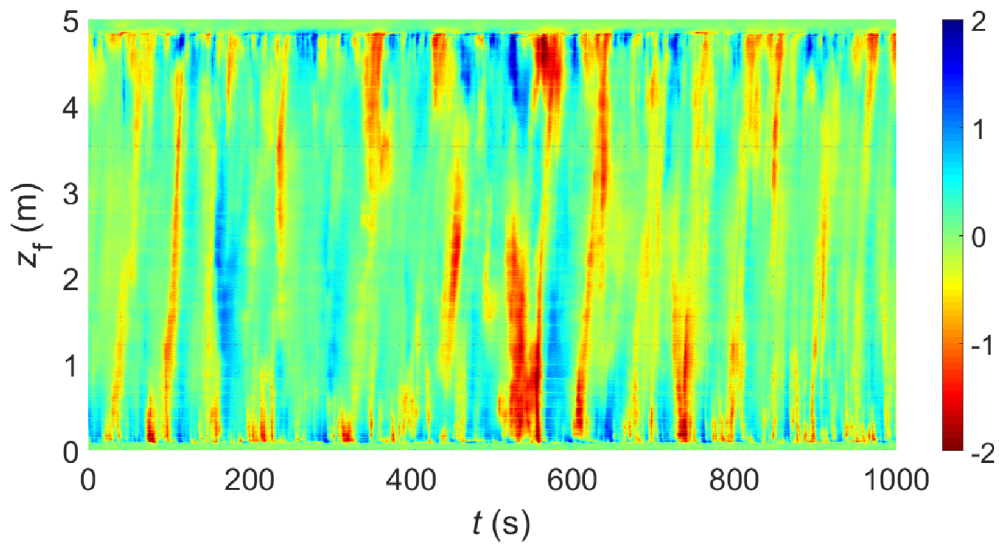
In this section will be evaluate correlation functions from ODiSI-B measurement to find out some of the wind (LSC) properties.

3.4.1 Detrended frequency shift

To acquire only temperature fluctuations along the fibre sensor and prepare data for the correlation computation, we removed the piecewise linear trend from the data by using a Matlab function called `detrend`. The time piece of `detrend` was 1080 s - every 5400 s dataset was divided to 5 sections. Temperature fluctuations Δf_{det} along the fibre sensor can be seen in the fig. 3.19a for central axis and in fig. 3.19b for side position, $\Delta T = 20^\circ\text{C}$. Again the 1000 s time windows are plotted at horizontal axis, position z_f on the optical fibre sensor is plotted at vertical axis and fluctuations are depicted by colours, where the red colour corresponds to the lowest frequency shift fluctuations - the highest temperature fluctuations and vice versa for blue colours. At side position, fluctuations are stronger, which corresponds with the location of the fibre sensor in the region of rising flow of LSC.

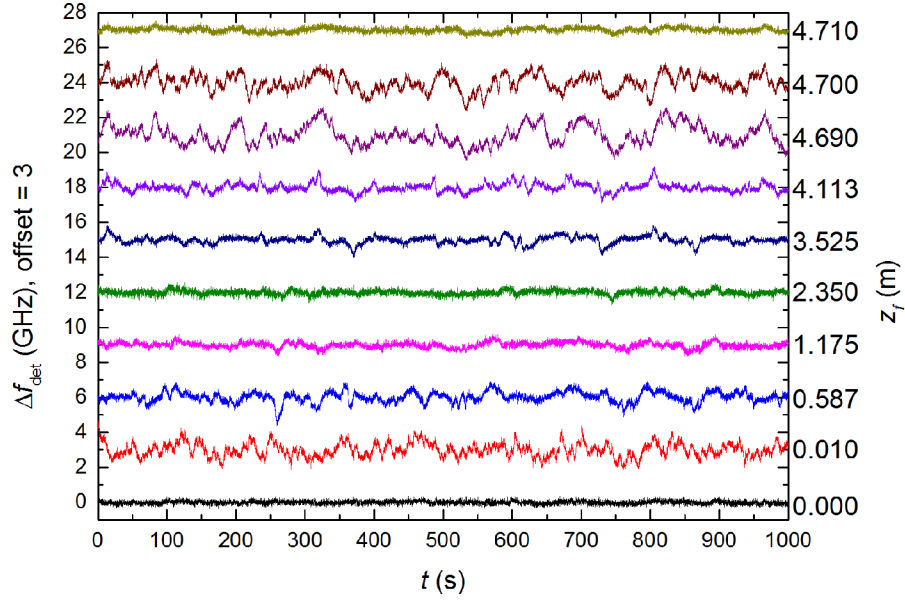


(a)

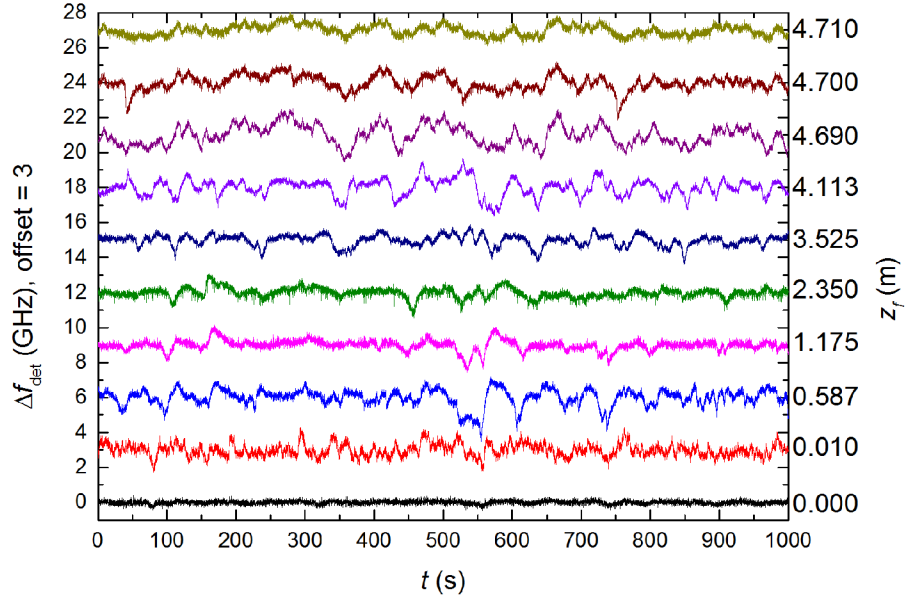


(b)

Fig. 3.19: Detrended frequency shift Δf_{det} for 20 °C a) run 2 - central axis, b) run 3 - side axis. The horizontal axis shows time window of 1000s, vertical axis depicts the position z_f at the optical fibre sensor and detrended frequency shift is shown by colours. The lowest frequency shift - the highest temperatures are depicted by red colours and vice versa for blue colours. a) We can see nearly vertical structures of warm (red and yellow) blurred strips with the repetition time of about 110s. b) The repetition time of blurred strips is about 70s at side position in uprising flow. The observed inclination of strips means that upper part of the fibre sensor is warmed (or cooled) later than its lower part, with the delay of about half of strips repetition time (~ 30 s). Extremal temperatures, both hot and cold, are near each plate. At middle the temperatures are rather moderate.



(a)



(b)

Fig. 3.20: Detrended frequency shift Δf_{det} at selected locations as function of time for 20°C a) run 2 - central axis, b) run 3 - side axis. The horizontal axis shows time window of 1000s. Positions z are depicted at right vertical axis. Individual positions are shifted by offset of 3. a) Δf_{det} fluctuates weakly at positions near the plates and in the middle of the cell ($z = 2.350$ m). The position $z = 4.710$ m corresponds to the hole in the cooling plate for fibre sensor entrance to the cell, which probably little altered the structure of the BL at this position. b) At both $z = 2.350$ m and $z = 4.710$ m the Δf_{det} fluctuates much more than in the core at the central axis.

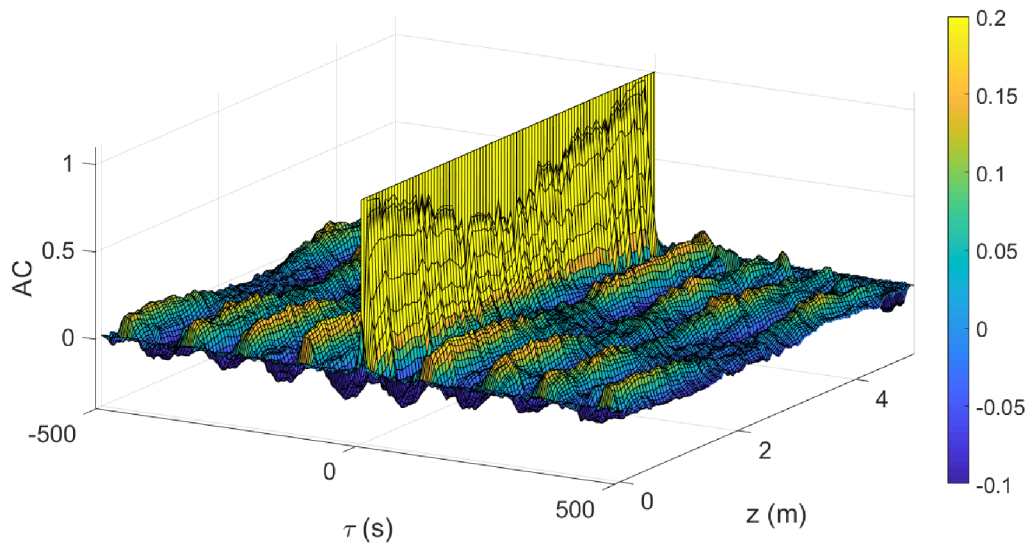
3.4.2 Autocorrelation and crosscorrelation

Correlation functions CC were computed from the detrended signals in fig. 3.20 by Matlab function $CC_{xy}(\tau) = \text{xcorr}(X, Y) = E(X_{n+m}Y_n^*) = E(X_nY_{n-m}^*)$, where X and Y are signals in different positions x, y along the fibre sensor. The time delay $\tau = m/f$, f is the sampled frequency, m is the index of sample, N is a number of the samples and $-N < m < N$, index $n = 1 \dots N$, asterisk denotes complex conjugation and E expresses the mean value [40]. Since ODiSI-B measured only real values of signal $Y = Y^*$. Autocorrelation is computed as $\text{xcorr}(X, X)$. In the case of presented crosscorrelation, the signals X are taken from the upper (colder) part of the cell ($z > 2.35$) while Y are time record from the lower (hot) part $z < 2.35$. Positions of the signal Y in CC calculations have mirror symmetry with the respect to the horizontal middle plane of the cell. Crosscorrelation function is calculated at each position z' from 0 to $L/2$ as $CC(\tau, z') = \text{xcorr}(X(z_f = L/2 + z'), Y(z_f = L/2 - z'))$, where z_f is the position at optical fibre sensor.

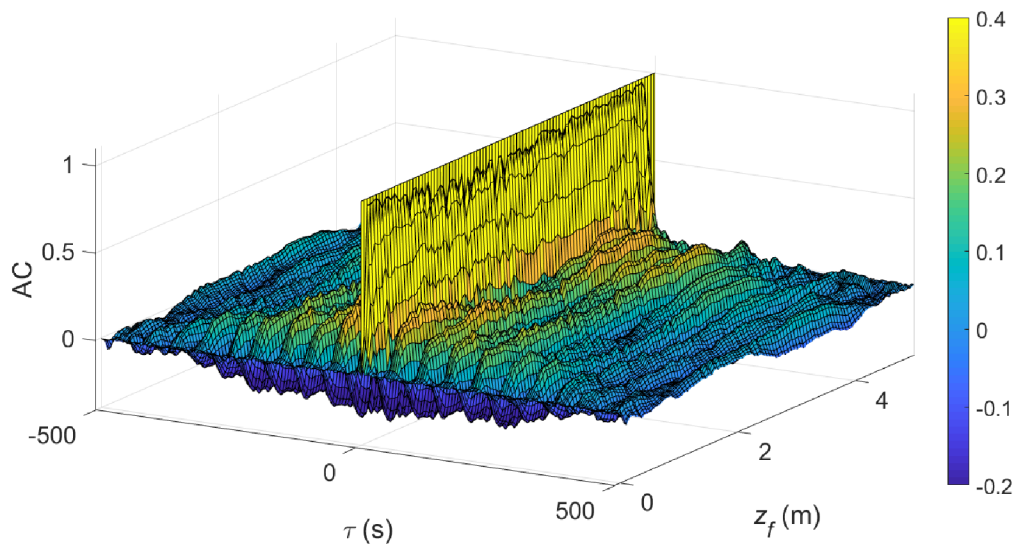
First figure 3.21 is shown only to introduce a rough idea about the structure of autocorrelation coefficient $AC = CC_{xx}$. Figure 3.22 presents top view of two previous figures. In these figures it is clearly visible, that the distance between neighbouring peaks of autocorrelation function is ~ 120 s along the cell axis and about two times shorter than near the sidewall (~ 55 s). Both values approximately correspond with repetition time of warm strips observed in fig. 3.20. AC at selected positions from fig. 3.22 are plotted in fig. 3.23.¹

Crosscorrelation function CC is plotted in the fig. 3.24, 3.25. Structure of these figures is similar, but the distance z' is now measured from the middle height of the cell. Crosscorrelation was always computed from signals equally distant from middle plane of the cell. First fig. 3.24 again gives an only rough image of the structure of the crosscorrelation coefficient in dependence on the τ and distance z' from the middle plane. At the distance $z' = 0$, the coefficient is very near to 1, because the signals are very close to each other, they approach autocorrelation function. Selected locations from the plots are shown in the fig. 3.26. Two very interesting phenomena visible in the fig. 3.25 are splitting of crosscorrelation function at the plates in the central position and inclination of the crosscorrelation function in τ at side position.

¹At lag $\tau = 0$ we can see sharp spikes in AC functions (3.21 and 3.23) which are characteristics of random signal ("white noise"). These are conspicuous especially for records taken in the core (middle axis, $z_f = 2.35$ m, fig. 3.23a) and always where the fluctuations of recorded signal are small (see also fig. 3.20a). This fact we interpret as contribution of background noise of the measurement method.

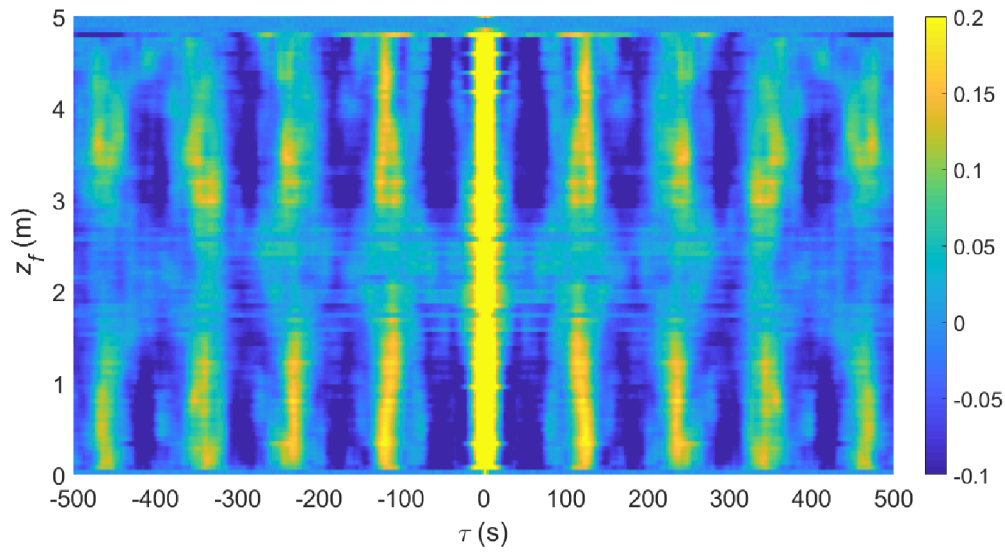


(a)

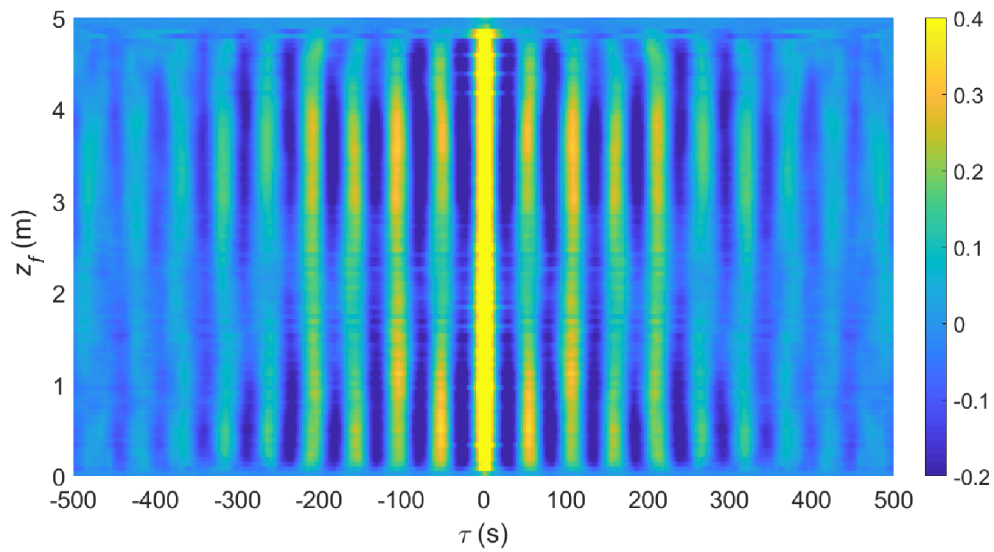


(b)

Fig. 3.21: Autocorrelation function AC for 20°C , a) central axis, b) side position. Lag τ and the distance z_f along the fibre sensor are depicted at horizontal axes. The value of autocorrelation is depicted on the vertical axis as well as colours. The span of the colour bar was lower to highlight lesser peaks - all values > 0.2 (0.4) are bright yellow and all values < -0.1 (-0.2) are dark blue for central axis (side position). This figure gives a rough idea of autocorrelation function structure. Top views of the plots are in the fig. 3.22.

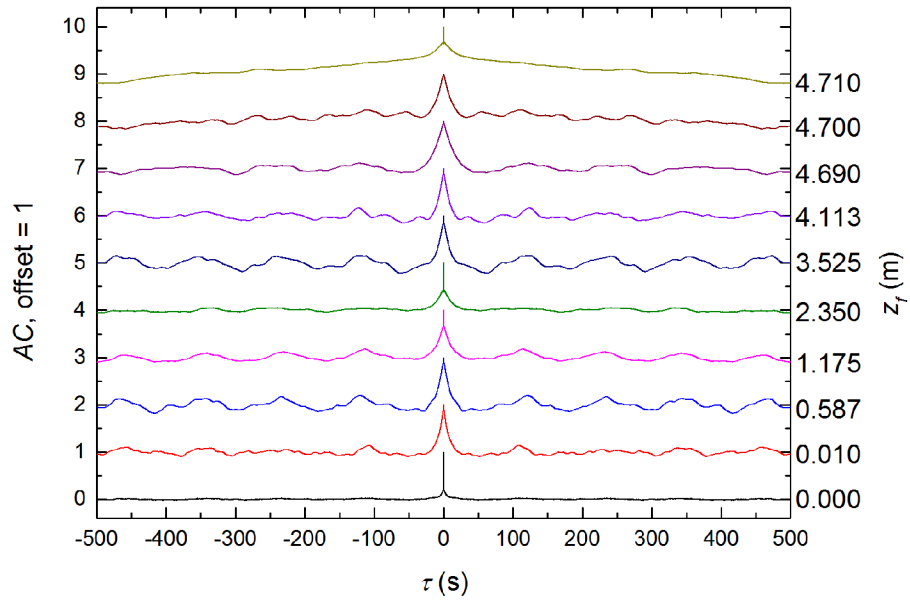


(a)

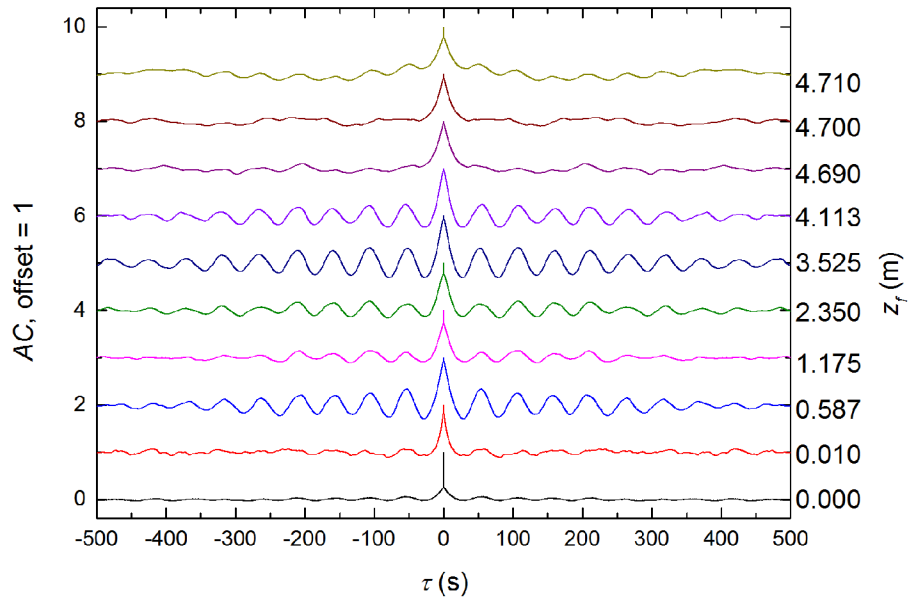


(b)

Fig. 3.22: Autocorrelation function for 20 °C, a) central axis b) side position. Horizontal axis shows time delay τ (lag) between a correlated phenomena, vertical axis depicts the distance z from the heating plate. The intensity of autocorrelation is depicted by colours. Span of the colour bar was lower to highlight lesser peaks - all values > 0.2 (0.4) are bright yellow and all values < -0.1 (-0.2) are dark blue for central axis (side position). Due to high computational demands on visualization only every 30th point in *lag* was plotted from the calculated values.

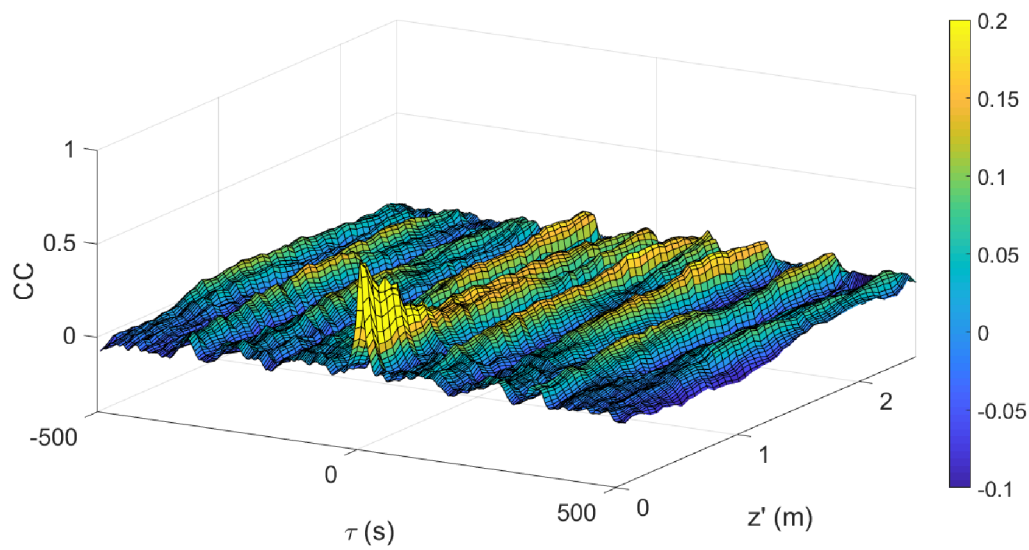


(a)

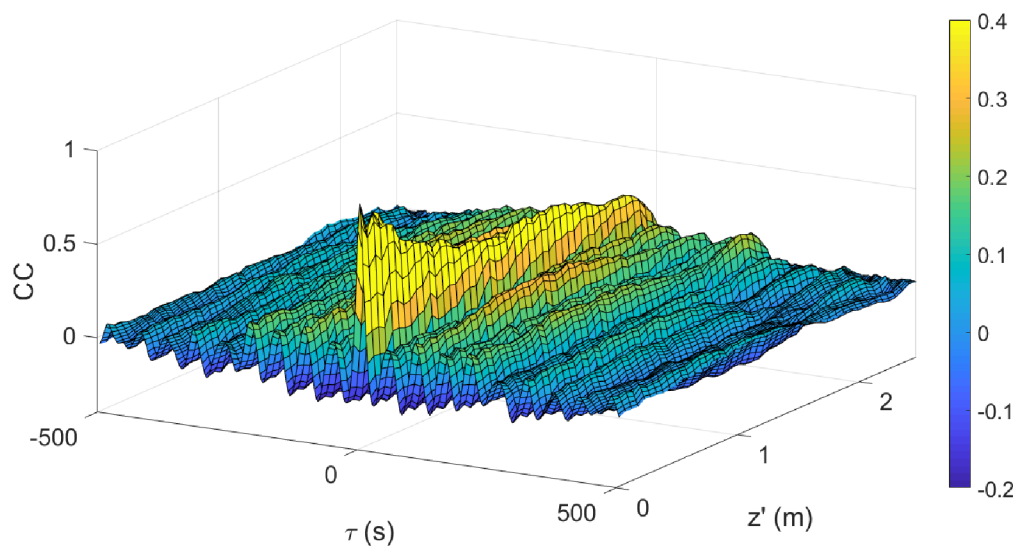


(b)

Fig. 3.23: Autocorrelation function AC for selected locations as a function of lag τ for 20°C , a) central axis, b) side position. Individual non-dimensional positions are shifted by offset 1 and depicted at right vertical axis.

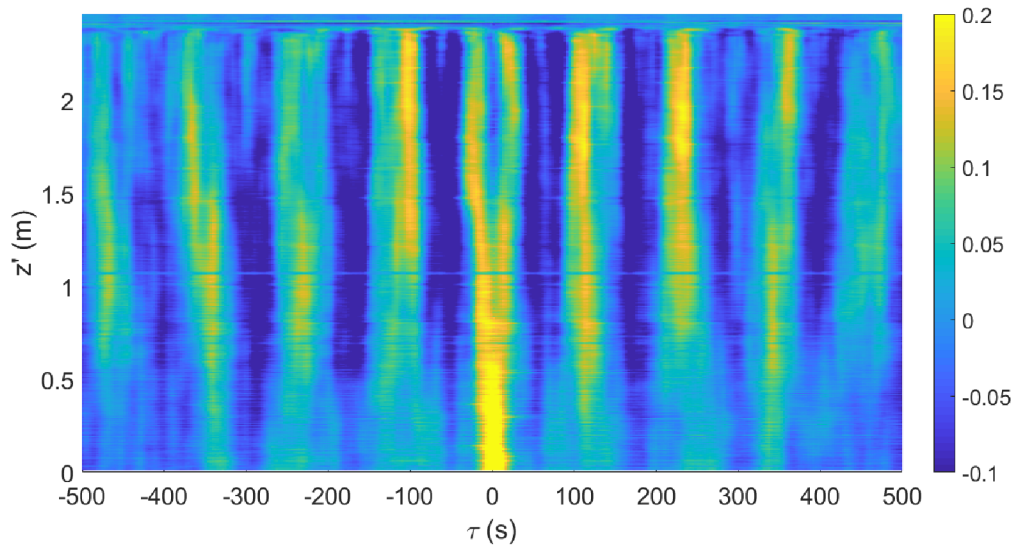


(a)

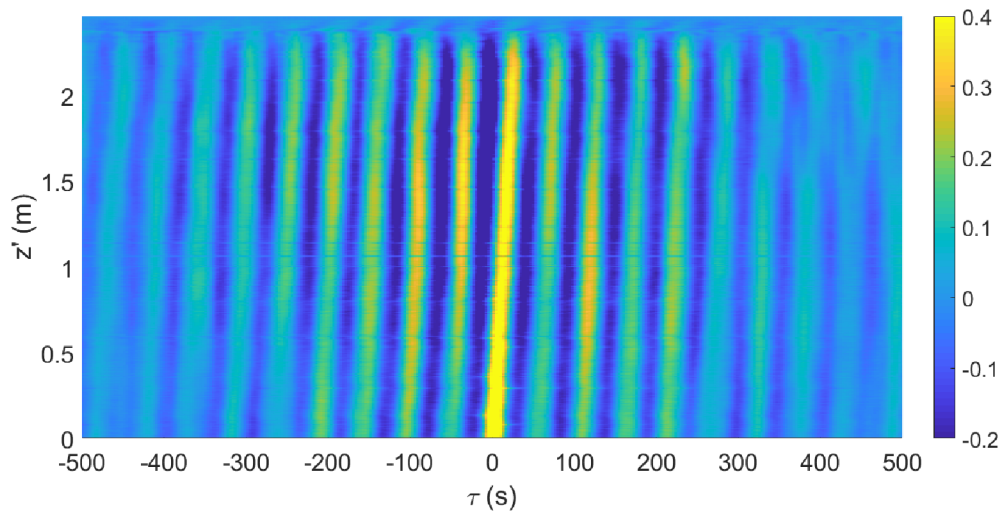


(b)

Fig. 3.24: Dependence of crosscorrelation coefficient CC on τ and distance z' for 20°C a) central axis b) side position. Crosscorrelation was always computed from signals equally distant from middle horizontal plane of the cell. The span of the colour bar was lower to highlight lesser peaks - all values > 0.2 (0.4) are bright yellow and all values < -0.1 (-0.2) are dark blue for central axis (side position). Top view of this figure is in the fig. 3.25.

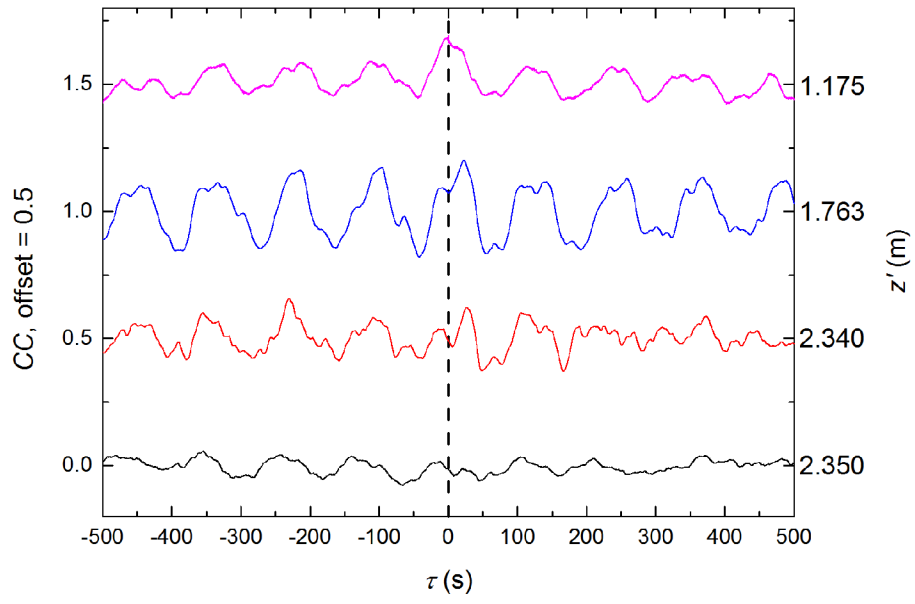


(a)

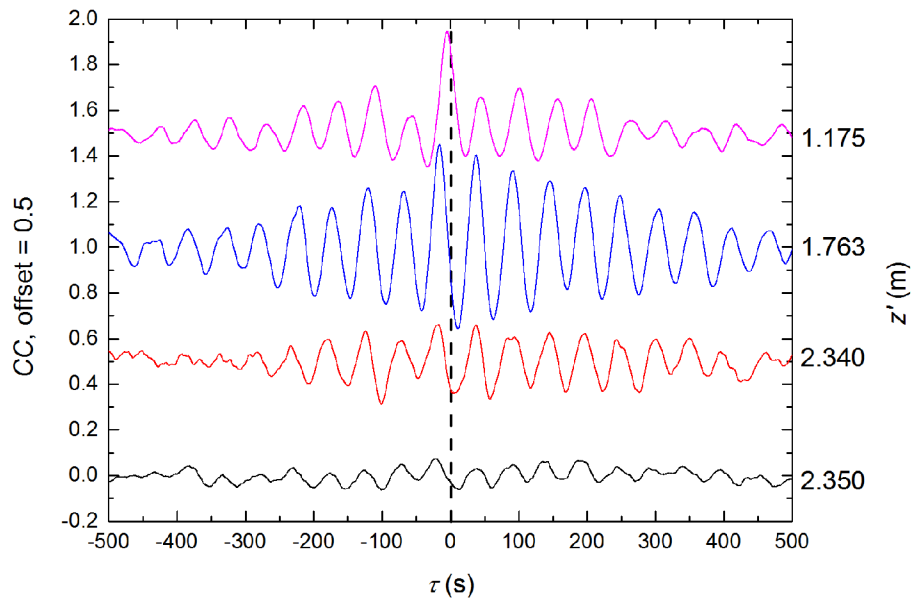


(b)

Fig. 3.25: Dependence of crosscorrelation coefficient CC on τ and distance z' from the vertical middle of the cell for 20°C a) central axis b) side position from top view. Span of the colour bar was lower to highlight lesser peaks - all values > 0.2 (0.4) are bright yellow and all values < -0.1 (-0.2) are dark blue for central axis (side position). a) Notice the split of crosscorrelation function in the BL region. b) Notice the inclination of the higher correlated structures from the vertical axis.



(a)



(b)

Fig. 3.26: Dependence of crosscorrelation coefficient CC on τ for selected distances z' from the horizontal middle plane of the cell for $\Delta T = 20^\circ\text{C}$ and a) central axis, b) side position.

3.4.3 Characteristics of coherent structures

We observed coherent structures of temperature field in RBC flow as periodically repeated peaks (maxima and minima) in autocorrelation (AC) and crosscorrelation (CC) functions. Data were obtained and processed for all measurements. In this work, we present results for $\Delta T = 20^\circ\text{C}$.

Regular structure of peaks was observed along the all height of the cell and within the time span at least 500 s (correlation between events up to 500 s or even more distant from each other was observed). See figs. 3.21 - 3.26.

Four time periods characterizing coherent structures of temperature field were observed. Time period of maxima (minima) repetition in AC and CC of temperature fluctuations ~ 53 s (side position, along the whole cell height) and ~ 110 s (central position, along the whole cell height). Time lag between neighbouring maxima (minima) in CC of the records taken at plates ~ 30 s at side position. Time distance between peaks in doublets in CC of the records taken at plates $\sim 40 - 50$ s at central axis.

It was found in the previous experiment [21], that typical LSC wind velocity in BOI is $v = 0.35$ m/s at $Ra = 5.2 \times 10^{10}$, $\Gamma = 2.00$. If we account the same speed for $\Gamma = 1.5$, period of LSC circulation for rectangular path along the side walls can be obtained as $T_{LSC} = (2D + 2L)/v = (2 \times 7.15 + 2 \times 4.7)/0.35 = 67$ s. In our case this time will be probably little lower, due to higher Ra number in most of experiments (higher velocity of the flow). From measurements of several temperatures at the side walls in other works (for a review see for example [7]) it was found out that in a cell with $\Gamma = 1$, LSC dynamics consists of two coherent oscillations (sloshing and twisting) characterized with one common period. Interpretation of time constants of here observed structures in AC and CC should be done in comparison with the results of other works studying dynamics of RBC flow and with the results obtained in this experiment for other Rayleigh numbers. This exceeds frame of this work.

4 SUMMARY AND CONCLUSIONS

This work is a first experiment utilizing Optical Distributed Sensor Interrogator Luna ODiSI-B for measurements of temperature profiles and temperature fluctuations in Rayleigh-Bénard convection across the whole height of the experimental cell, involving the turbulent core and the region of the thermal boundary layers. Measurements were conducted in Barrel of Ilmenau (BOI) in Germany, containing the cylindrical experimental cell with a diameter of 7.15 m and the height of 4.7 m (the aspect ratio $\Gamma = 1.5$) The cell is filled with dry air used as a working fluid. Data were post-processed at Institute of Scientific Instruments (ISI) of the CAS.

The Luna ODiSI-B should enable to measure the temperature profile with a high spatial resolution of 5 mm and profiles frequency up to 100 Hz along a very thin glass optical fibre sensor with the length of 5 m. This system has not yet been used in any RBC experiments in the past and the temperature profiles in RBC have not yet been measured along the full cell height instantaneously and with such high spatial resolution in any laboratory.

The Luna ODiSI-B system was supplemented with two vertically movable Pt100 probes specially designed at the Institute of Scientific Instruments of the CAS (ISI) for reference measurements of the temperature profiles. The lower Pt100 probe was used for the measurement in the region of the bottom boundary layer and turbulent core, the upper Pt100 probe was used only for measurement in the region of the top boundary layer. Both Pt100 probes were suspended on the feed cables passing through the hole in the top plate. The probes could be moved by hand via cables up and down.

The measurements using of both techniques, Luna ODiSI-B and Pt100 probes, were performed at two verticals: along the cell axis and a vertical line displaced 1.4 m from the side wall (side position). The Rayleigh number Ra during the measurements span from 1×10^{10} to 2×10^{11} .

Temperature profiles, measured by two movable Pt100 probes at $Ra = 5.45 \times 10^{10}$ well agreed with detail measurements of boundary layers (BLs) temperature profiles recorded in [21] at BOI. Profiles measured at side position were compared to data from Goettingen (SF_6) obtained in the vicinity of the side wall [37]. Asymmetry of BL layers due to NOB effects was observed both in the measurements of core temperatures T_c and the temperature profiles. The recorded temperature T_c at $\Delta T > 5^\circ\text{C}$ was in all cases higher than mean temperature T_m . This does not correspond with predictions for gases stated in section 1.4.

Raw (uncalibrated) frequency shift signals were used for evaluation of autocorrelation and crosscorrelation function between time records at positions symmetrical with respect to the middle horizontal plane of the cell. We found four characte-

istic times of coherent structures of the temperature field. Interpretation of these results exceeds the frame of this work. In the thesis are presented only data obtained for $\Delta T = 20^\circ\text{C}$. All experimental data, processed data and Matlab scripts used for processing were published in the EuHIT database TurBase, which should be freely accessible to other laboratories interested in turbulence and heat transfer research. Preliminary results were also published in [12]. At this moment, the usability of ODiSI-B for temperature profile measurements in cryogenic helium RBC experiment in ISI is being considered.

BIBLIOGRAPHY

- [1] E. Fonda and K. R. Sreenivasan, “Turbulent Thermal Convection,” in *Selected Topics of Computational and Experimental Fluid Mechanics*. Springer International Publishing, 2015, pp. 37–49. [Online]. Available: <http://link.springer.com/10.1007/978-3-319-11487-3>
- [2] G. Ahlers, “Turbulent convection,” *Physics*, vol. 2, p. 74, sep 2009. [Online]. Available: <http://link.aps.org/doi/10.1103/Physics.2.74>
- [3] F. Chillà and J. Schumacher, “New perspectives in turbulent Rayleigh-Bénard convection,” *The European Physical Journal E*, vol. 35, no. 7, p. 58, 2012. [Online]. Available: <http://www.springerlink.com/index/10.1140/epje/i2012-12058-1>
- [4] K.-Q. Xia, “Current trends and future directions in turbulent thermal convection,” *Theoretical and Applied Mechanics Letters*, vol. 3, no. 5, pp. 1–10, 2013. [Online]. Available: <http://linkinghub.elsevier.com/retrieve/pii/S2095034915302531>
- [5] J. Zhang, S. Childress, and A. Libchaber, “Non-Boussinesq effect: Thermal convection with broken symmetry,” *Physics of Fluids*, vol. 9, no. 4, pp. 1034–1042, 1997. [Online]. Available: <http://scitation.aip.org/content/aip/journal/pof2/9/4/10.1063/1.869198>
- [6] R. du Puits, C. Resagk, A. Tilgner, F. Busse, and A. Thess, “Structure of thermal boundary layers in turbulent Rayleigh-Bénard convection,” *Journal of Fluid Mechanics*, vol. 572, pp. 231–254, 2007. [Online]. Available: http://www.journals.cambridge.org/abstract_S0022112006003569
- [7] V. Musilová, T. Králík, M. La Mantia, M. Macek, P. Urban, and L. Skrbek, “Reynolds number scaling in cryogenic turbulent Rayleigh-Bénard convection in a cylindrical aspect ratio one cell,” *Journal of Fluid Mechanics*, vol. 832, pp. 721–744, 2017. [Online]. Available: https://www.cambridge.org/core/product/identifier/S0022112017006383/type/journal_article
- [8] R. H. Kraichnan, “Stochastic models for many-body systems. II. Finite systems and statistical nonequilibrium,” *Journal of Mathematical Physics*, vol. 3, no. 3, pp. 496–521, 1962. [Online]. Available: <http://aip.scitation.org/doi/10.1063/1.1724249>

- [9] “ScaRaB - Scaling and temperature profiles in turbulent Rayleigh-Bénard convection - EuHIT Project — EuHIT.” [Online]. Available: <https://www.euhit.org/projects/ScaRaB> (Accessed 2018-05-22).
- [10] Y. Wang, X. He, and P. Tong, “Boundary layer fluctuations and their effects on mean and variance temperature profiles in turbulent Rayleigh-Bénard convection,” *Physical Review Fluids*, vol. 1, no. 8, 2016.
- [11] “TurBase.” [Online]. Available: https://turbase.cineca.it/init/routes/#!/logging/view_dataset/96/tabmeta (Accessed 2018-05-07).
- [12] J. Drahotský, P. Hanzelka, V. Musilová, M. Macek, R. Puits, and P. Urban, “Temperature profiles measurements in turbulent Rayleigh-Bénard convection by optical fibre system at the Barrel of Ilmenau,” *EPJ*, vol. Will be published, 2017.
- [13] COMSOL, “Multiphysics Cyclopedia.” [Online]. Available: <https://www.comsol.com/multiphysics> (Accessed 2018-02-09).
- [14] A. Pandey, A. Kumar, A. G. Chatterjee, and M. K. Verma, “Dynamics of large-scale quantities in Rayleigh-Bénard convection,” *Physical Review E*, vol. 94, no. 5, 2016. [Online]. Available: <http://arxiv.org/abs/1611.09071>
- [15] G. Ahlers, E. Brown, F. F. Araujo, D. Funfschilling, S. Grossmann, and D. Lohse, “Non-Oberbeck-Boussinesq effects in strongly turbulent Rayleigh-Bénard convection,” *Journal of Fluid Mechanics*, vol. 569, pp. 409–445, 2006. [Online]. Available: http://www.journals.cambridge.org/abstract_S0022112006002916
- [16] G. Ahlers, F. F. Araujo, D. Funfschilling, S. Grossmann, and D. Lohse, “Non-Oberbeck-Boussinesq Effects in Gaseous Rayleigh-Bénard Convection,” *Physical Review Letters*, vol. 98, no. 5, pp. 1–4, 2007. [Online]. Available: <http://link.aps.org/doi/10.1103/PhysRevLett.98.054501>
- [17] L. Skrbek and P. Urban, “Has the ultimate state of turbulent thermal convection been observed?” *Journal of Fluid Mechanics*, vol. 785, pp. 270–282, 2015. [Online]. Available: http://www.journals.cambridge.org/abstract_S0022112015006382
- [18] H. Schlichting and K. Gersten, *Boundary-Layer Theory*. Berlin, Heidelberg: Springer Berlin Heidelberg, 2017. [Online]. Available: <http://link.springer.com/10.1007/978-3-662-52919-5>

- [19] X. Z. Wu and A. Libchaber, “Non-Boussinesq effects in free thermal convection,” *Physical Review A*, vol. 43, no. 6, pp. 2833–2839, 1991. [Online]. Available: <http://link.aps.org/doi/10.1103/PhysRevA.43.2833>
- [20] “The Barrel of Ilmenau.” [Online]. Available: <https://www.tu-ilmenau.de/en/barrel-of-ilmenau/external-users/> (Accessed 2018-02-13).
- [21] R. D. Puits, C. Resagk, and A. Thess, “Thermal boundary layers in turbulent Rayleigh–Bénard convection at aspect ratios between 1 and 9,” *New Journal of Physics*, vol. 15, no. 1, pp. 1–22, 2013. [Online]. Available: <http://stacks.iop.org/1367-2630/15/i=1/a=013040?key=crossref.c37267551e705fbb4213f0d73ac70f54>
- [22] R. Kaiser and R. du Puits, “Local wall heat flux in confined thermal convection,” *International Journal of Heat and Mass Transfer*, vol. 73, pp. 752–760, 2014. [Online]. Available: <http://dx.doi.org/10.1016/j.ijheatmasstransfer.2014.02.033>
- [23] D. Samiec, “Distributed fiber-optic temperature and strain measurement with extremely high spatial resolution,” *Photonik 2012*, pp. 10–13, 2012.
- [24] *User’s Guide, ODISI-B v. 5.0.0*, 2007.
- [25] Sensuron, “Introduction to Fiber Optic Sensing,” pp. 1–39, 2016. [Online]. Available: <http://cdn.sensuron.com/wp-content/uploads/2016/06/Introduction-to-Fiber-Optic-Sensing.pdf>
- [26] S. Lomperski, C. Gerardi, and D. Lisowski, “Fiber Optic Distributed Sensors for High-resolution Temperature Field Mapping,” *Journal of Visualized Experiments*, 2016. [Online]. Available: <http://www.jove.com/video/54076/fiber-optic-distributed-sensors-for-high-resolution-temperature-field>
- [27] Datasheet, “ODiSI-B Optical Distributed Sensor Interrogator.” [Online]. Available: http://lunainc.com/wp-content/uploads/2016/07/ODB5-DataSheet_Rev13_020217.pdf
- [28] C. Crunelle, S. Member, M. Legré, M. Wuilpart, P. Mégret, and N. Gisin, “Distributed Temperature Sensor Interrogator Based on Polarization-Sensitive Reflectometry,” vol. 9, no. 9, pp. 1125–1129, 2009.
- [29] RP Photonics, “Encyclopedia of Laser Physics and Technology - Rayleigh scattering, optical fibers, propagation loss.” [Online]. Available: https://www.rp-photonics.com/rayleigh_scattering.html (Accessed 2018-02-25).

- [30] L. Palmieri and L. Schenato, “Distributed Optical Fiber Sensing Based on Rayleigh Scattering,” *The Open Optics Journal*, vol. 7, no. 24, pp. 104–127, 2013. [Online]. Available: <https://benthamopen.com/contents/pdf/TOOPTSJ/TOOPTSJ-7-104.pdf>
- [31] M. Wegmuller, P. Oberson, J. P. von der Weid, O. Guinnard, L. Guinnard, C. Vinegoni, M. Legre, and N. Gisin, “Overview of coherent reflectometry techniques: characterization of components and small systems,” *Technical Digest Symposium on Optical Fiber Measurements, 2000 (NIST SP 953)*, pp. 155–160, 2000. [Online]. Available: http://www.unige.ch/gap/quantum/_media/publications:bib:0155wegm.pdf
- [32] J. P. Von Der Weid, R. Passy, G. Mussi, and N. Gisin, “On the characterization of optical fiber network components with optical frequency domain reflectometry,” *Journal of Lightwave Technology*, vol. 15, no. 7, pp. 1131–1141, 1997.
- [33] K. Yuksel, M. Wuilpart, V. Moeyaert, and P. Megret, “Optical frequency domain reflectometry: A review,” *2009 11th International Conference on Transparent Optical Networks*, no. June, pp. 1–5, 2009. [Online]. Available: <http://ieeexplore.ieee.org/document/5185111/>
- [34] Z. Ding, C. Wang, K. Liu, J. Jiang, D. Yang, G. Pan, Z. Pu, and T. Liu, “Distributed Optical Fiber Sensors Based on Optical Frequency Domain Reflectometry: A review,” *Sensors*, vol. 18, no. 4, pp. 1–31, 2018. [Online]. Available: <http://www.mdpi.com/1424-8220/18/4/1072>
- [35] “Typ 03001, 03002 — ZPA EKOREG, spol. s r.o. — CZ.” [Online]. Available: <http://www.zpaul.cz/blog/wpcproduct/typ-03001-03002/> (Accessed 2018-05-22).
- [36] G. Ahlers, E. Bodenschatz, D. Funfschilling, S. Grossmann, X. He, D. Lohse, R. J. A. M. Stevens, and R. Verzicco, “Logarithmic Temperature Profiles in Turbulent Rayleigh–Bénard Convection,” *Physical Review Letters*, vol. 109, no. 11, pp. 1–5, 2012. [Online]. Available: <https://link.aps.org/doi/10.1103/PhysRevLett.109.114501>
- [37] G. Ahlers, E. Bodenschatz, and X. He, “Logarithmic temperature profiles of turbulent Rayleigh–Benard convection in the classical and ultimate state for a Prandtl number of 0.8,” *Journal of Fluid Mechanics*, vol. 758, pp. 436–467, 2014. [Online]. Available: http://www.journals.cambridge.org/abstract_S0022112014005436

- [38] Q. Zhou, R. J. a. M. Stevens, K. Sugiyama, S. Grossmann, D. Lohse, and K.-Q. Xia, “Prandtl-Blasius temperature and velocity boundary layer profiles in turbulent Rayleigh-Bénard convection,” *Journal of Fluid Mechanics*, vol. 664, pp. 297–312, 2010. [Online]. Available: <http://arxiv.org/abs/1002.1339>
- [39] Luna, “Distributed Fiber Optic Sensing: Temperature Coefficient for Polyimide Coated Low Bend Loss Fiber, in the 10 C - 80 C range,” *Engineering Note*, pp. 1–12, 2014.
- [40] “Cross-correlation - MATLAB xcorr.” [Online]. Available: <https://www.mathworks.com/help/signal/ref/xcorr.html> (Accessed 2018-05-21).

LIST OF SYMBOLS, PHYSICAL CONSTANTS AND ABBREVIATIONS

T	<i>Temperature</i>
T_p	<i>Planar average temperature</i>
T_m	<i>Mean temperature</i>
λ_T	<i>Thickness of the thermal boundary layers</i>
z	<i>Height from the bottom plate</i>
T_c	<i>Core temperature</i>
T_t	<i>Temperature of the top - cooling plate</i>
T_b	<i>Temperature of the bottom - heating plate</i>
ΔT	<i>Temperature difference between the plates</i>
ρ	<i>Density</i>
Δ_t	<i>Temperature drop at top boundary layer</i>
Δ_b	<i>Temperature drop at bottom boundary layer</i>
λ_t	<i>Thickness of the top boundary layer</i>
λ_b	<i>Thickness of the bottom boundary layer</i>
χ	<i>Parameter of asymmetry of BL layers</i>
μ	<i>Shear - dynamic viscosity</i>
u	<i>Flow velocity</i>
t	<i>Time</i>
p	<i>Fluid pressure</i>
g	<i>Gravitational acceleration</i>
α	<i>Coefficient of thermal expansion</i>
P	<i>Pressure shift</i>
ν	<i>Kinematic viscosity</i>

κ	<i>Thermal diffusivity</i>
Re	<i>Reynolds number</i>
U	<i>Free fall velocity</i>
L	<i>Height of the cell</i>
Ra	<i>Rayleigh number</i>
Pr	<i>Prandtl number</i>
Nu	<i>Nusselt number</i>
h	<i>Convective heat transfer coefficient</i>
Γ	<i>Aspect ratio</i>
D	<i>Diameter of the cell</i>
I	<i>Intensity</i>
λ	<i>Wavelength</i>
T_{Pt}	<i>Temperature of the Pt100 probe</i>
σ_{Pt}	<i>Standard deviation of the Pt100 probe</i>
Θ	<i>Non-dimensional temperature</i>
ξ	<i>Non-dimensional radial position</i>
Δf	<i>Frequency shift</i>
T_{Cal}	<i>Temperature used for calibration</i>
AC	<i>Autocorrelation function</i>
CC	<i>Crosscorrelation function</i>
τ	<i>Lag of correlation function</i>
z_f	<i>Distance along the fibre sensor from the heating plate</i>
z'	<i>Distance from the vertical centre of the cell</i>

BL *Boundary layers*

BOI *Barrel of Ilmenau*

CAS *Czech Academy of Science*

c-OFDR *Coherent Optical Frequency-domain Reflectometry*

DOFS *Distributed optical fibre sensing*

EuHIT *European High-Performance Infrastructures in Turbulence*

FFT *Fast Fourier transform*

ISI *Institute of Scientific Instruments of the CAS*

LSC *Large scale wind*

NOB *Non-Oberbeck-Boussinesq*

NS *Navier-Stokes*

OB *Oberbeck-Boussinesq*

ODiSI-B *Optical Distributed Sensor Interrogator from Luna Innovations company*

RBC *Rayleigh-Bénard convection*

SF₆ *Sulfur hexafluoride*

